Fundamental Theoretical Investigations of the Photocatalytic deNO$_x$ Reactions over TiO$_2$ Surfaces

Submitted in partial fulfillment of the requirements for the degree of Doctor rerum naturalium in physics in the

Bremen Center for Computational Material Science

University of Bremen

by

Pu Guo

Primary supervisor: Thomas Frauenheim

Secondary supervisor: Peter Deák

Date of the doctoral colloquium: 22.12.2022

June, 2022

DECLARATION

I, Pu Guo, declare that the thesis entitled " Fundamental Theoretical Investigations of the Photocatalytic deNO_x Reactions over TiO_2 Surfaces" submitted by me, for the award of the degree of *Doctor of physics* to University of Bremen is a record of bonafide work carried out by me.

I further declare that the work reported in this thesis has not been submitted and will not be submitted, either in part or in full, for the award of any other degree or diploma in this institute or any other institute or university.

Place: Bremen

Date: **Signature of the Candidate**

CERTIFICATE

This is to certify that the thesis entitled "Fundamental Theoretical Investigations of the Photocatalytic deNO_x Reactions over TiO_2 Surfaces" submitted by Pu Guo, Bremen Center for Computational Material Science, University of Bremen, for the award of the degree of *Doctor of physics*, is a record of bonafide work carried out by her under my supervision.

The contents of this report have not been submitted and will not be submitted either in part or in full, for the award of any other degree or diploma in this institute or any other institute or university. The thesis fulfills the requirements and regulations of the University and in my opinion meets the necessary standards for submission.

Place: Bremen

Date: **Signature of the Supervisor**

(Prof. Thomas Frauenheim)

ABSTRACT

Emissions of nitrogen oxides (NO_x) have a serious impact on our environment and human health. Photocatalytic denitrification ($deNO_x$) on titania attracted much attention due to it is low-cost and nonpolluting nature, but in reality undesired nitrite and nitrate were produced, instead of harmless N_2. Establishing the global activity and selectivity trend among active sites is an important base to explore and improve the $deNO_x$ processes. Herein, I have investigated the reaction mechanisms of NO_2 and H_2O on anatase $TiO_2(101)$ and the direct decomposition of NO on various TiO_2 surfaces. A polaron-corrected GGA functional (GGA + Lany-Zunger) was applied to improve the description of electronic states in photo-assisted process and a reaction phase diagram (RPD) was applied to understand the (quasi) activity trend over different active sites. In the $deNO_2$ process, it was found that the perfect surface exhibits high activity while the activity on defective surfaces is limited by the sluggish recombinative desorption. A photogenerated hole can weaken the OH* adsorption energies and circumvent the scaling relation of the dark reaction, ultimately significantly increasing the denitrification activity. In the deNO process, it was found that without illumination N_2 production is inactive over various TiO_2 surfaces/sites, and photo-generated holes can break the scaling relation of the dark condition by weakening O_2* adsorption, leading to a significant increase in deNO activity of defective titania surfaces. The low N_2 selectivity in experiments was further investigated by microkinetic modeling. It was found that the weak adsorption of N_2O led to the low N_2 selectivity on titania surfaces. On the contrary, the N_2 selectivity of Ti-modified zeolite was enhanced due to stronger N_2O* adsorption. I show here that the reaction phase diagram (RPD) analysis can clearly establish a global picture of reaction activity and selectivity over various catalytic sites. The reactivity can be tuned by illumination-induced localized charge. Combined with microkinetic modeling, it can effectively determine the kinetic limits. This study provides insights for improving the design of photocatalysts.

Keywords: *Photocatalysis*, *deNO$_x$*, *Reaction phase diagram (RPD)*, *GGA-LZ (Lany-Zunger) Functional*, *Microkinetic modeling*.

ACKNOWLEDGEMENT

With immense pleasure and deep gratitude, I am very grateful to **Prof. Thomas Frauenheim** for his kindness and encouragement, as well as everything he did for me during my stay in Germany, to **Prof. Peter Deák** and **Prof. Jianping Xiao** for their discussion and guidance of my work, and for their encouragement and patience in helping me to solve the problems I encountered in my work. This project would not have been successfully finished without their motivation and constant supervision.

I express my sincere thanks to **Dr. Bálint Aradi, Dr. Christof Köhler, Dr. Mauricio Chagas da Silva, Meisam Farzalipour Tabriz and Dr. Xiaoyan Fu** for their kindness and technological support on my work. I acknowledge the support rendered by my colleagues in Bremen group, Dalian group, QM3 group and Shenzhen group in several ways throughout my work.

I express my sincere thanks to my friends Jiaxin Li, Shuman Zhang and Zhijie Li for the endless discussions, supports and encouragements.

I wish to extend my profound sense of gratitude to my grandparents and my parents for all the sacrifices they made during my research and for their constant encouragement and moral support along with patience and understanding whenever needed.

I am grateful to the support from Chinese scholarship council (No. CSC201806 310123) and the support of the Supercomputer Center of Northern Germany (HLRN Grant No. hbc00049), providing me with infrastructural facilities and many other resources needed for my research.

Place: Bremen

Date: June, 2022 **Pu Guo**

TABLE OF CONTENTS

LIST OF FIGURES

LIST OF TABLES

1 Introduction

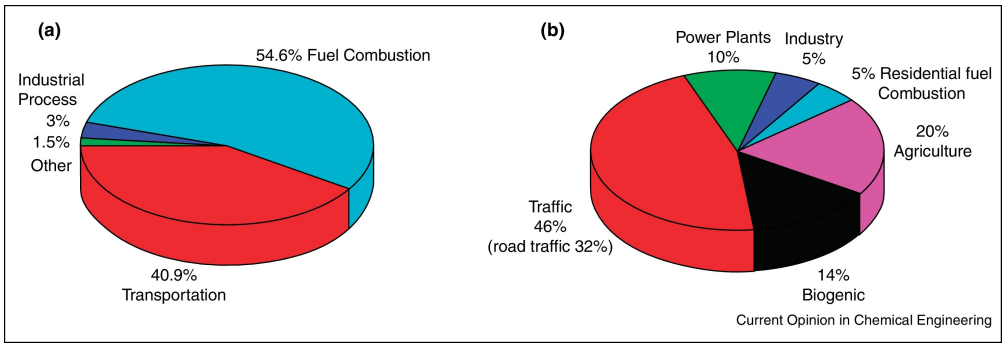

Fig. 1.1 Nitrogen oxide emissions by source category in (a) the United States and (b) European Countries[1].

NO_x, primarily NO and NO_2, are poisonous gases and have significant adverse effects on the environment and human beings. They mainly emitted into atmosphere through the combustion of fossil fuels as shown in **Fig. 1.1**. NO can be oxidized into NO_2 in the air during the combustion processes and NO_x can also lead to acid rain due to its low solubility in water[1]. In addition, NO_x also affects the indoor areas. It has been reported that NO_2 levels were 3-5 times higher in residential areas than rural area because of the cooking combustion[2].

With the increased interest toward removal of NO_x ($deNO_x$), various methods had been applied in $deNO_x$ process as shown in **Fig. 1.2**. The primary NO_x removal methods are carried out in the combustion zone without an additional reactor. NO_x production can be reduced by adjusting the combustion parameters, such as decreasing the temperature and the concentration of oxygen in the flame[2]. The prevailing secondary methods are selective catalytic reduction(SCR) and selective non-catalytic reduction(SNCR)[9]. Methods like NO absorption, phase separation[10], NO storage and reduction are all part of the other methods[2]. The main shortcoming of the secondary methods is that they must use additional equipment. Generally, the secondary methods are often more efficient in denitrification than primary methods[10, 2]. Photocatalysis is an attractive and promising technology for the removal of toxic and hazardous compounds[2]. There are three photocatalytic methods for photocatalytic denitrification: photo oxidation, photo selective catalytic reduction(photo-SCR), and photo

decomposition. Photo decomposition is an ideal process that does not take into account the presence of other compounds[2]. Therefore, NO_x can be oxidized to nitric acid in the presence of water or reduced to harmless N_2 in the photocatalytic deNO_x process.

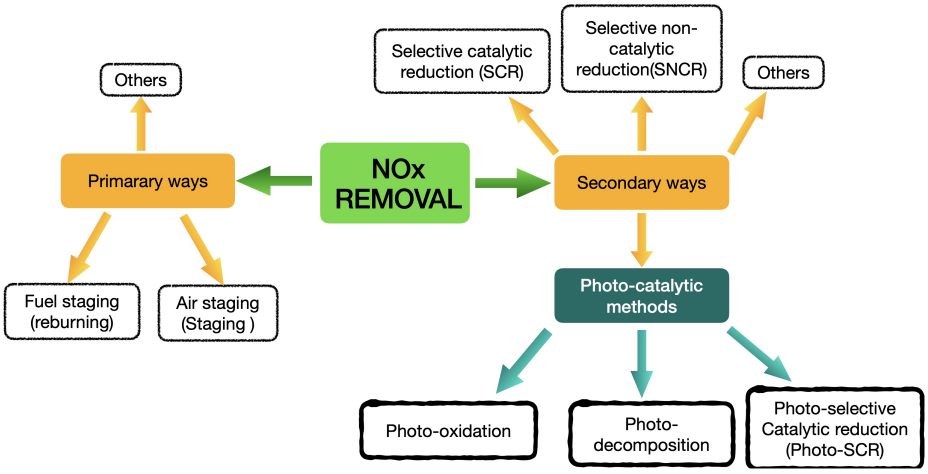

Fig. 1.2 The methods of NOx removal[2].

In the past decades, TiO_2 photocatalysis has been extensively researched, and the process has been commercialized in several fields[11, 12, 13, 14, 15, 16, 17]. Toma et al. suggested that NO_x conversions depend on the crystalline phase of TiO_2[18]. As shown in **Fig. 1.3a**, the conversions of NO and NO_x in nontreated Degussa P25 TiO_2 were about 33% and 18%, respectively. NO and NO_x conversions decrease as the temperature increase. The comparison of deNO_x mechanism between (anatase and rutile) titania surfaces can also provide useful guidance for catalyst design in the future. Thus, it is necessary to investigate the underlying effect of diverse crystalline phase of TiO_2 on photocatalytic deNO_x reactions.

Overall, the photocatalytic efficiency of TiO_2 is not high. Enormous efforts had been made to improve the performance of TiO_2, for example, by metal or metal oxide deposition, elemental doping and defect formation[4]. It's reported that nanoscale anatase TiO_2 and iron doped TiO_2 have shown higher NO removal capacities[4, 19]. As shown in **Fig. 1.3b**, when the light was turned on the reaction proceeded immediately, implying that the UV-illumination light is indispensable for the photocatalytic deNO_x reaction on reduced TiO_2[4]. Additionally, the deNO_x reaction mechanisms has been widely discussed, but it is still controversial. The details is presented in the main text. In this work, I attempt to clarify the chemical reactions mechanisms of deNO_x process and figure out the limits of it on diverse TiO_2 surfaces.

Computational catalyst design, based on electronic structure calculations, is becoming an important approach to provide guidance for the development of new materials with high activity and specific selectivity[5, 20, 21]. It is time consuming and hard to cover all possible reaction pathways if we study it in the traditional way. Therefore, it's

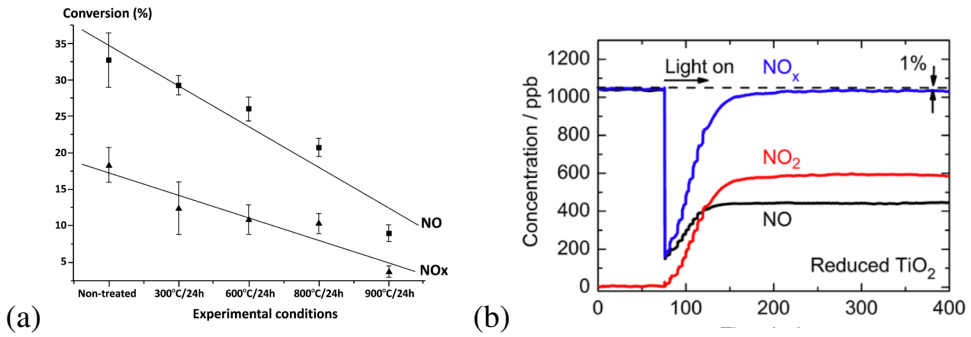

Fig. 1.3 (a) Influence of the TiO_2 annealing temperature on the photocatalytic conversion of nitrogen oxides, showing a negative correlation between the annealing temperature and the TiO_2 photocatalytic activity. Reprinted with kind permission from Springer Science and Business Media[3]. (b)Photocatalytic degradation of NO in air by reduced TiO_2 under UV light irradiation[4].

necessary to introduce an effective scheme to study a full set of reaction pathways. It was found that there are several linear correlations between adsorption energies of reactive adsorbates(e.g. C* vs CH_x*, described as: E_{ad} CH_x* = a × E_{ad} C* + b)(called scaling relations) over a series of catalysts (**Fig. 1.4a**)[5, 20, 22, 23, 24, 25, 26, 27], which can serve as the basis for reducing the dimensionality of complex reactions. One or two key adsorption energies can be chosen as descriptors to predict the activity trend. The well-known Sabatier principle can be quantitatively described through a volcano plot (**Fig. 1.4**) of rates calculated theoretically[21, 28, 29, 30, 31, 21, 32, 33, 34]. The term "volcano plot" comes from the shape of the curve describing the activity as a function of the absorption energy, which was chosen as descriptor. The activity of the catalysts/sites in the left leg of a volcano plot(such as A, B and C in **Fig. 1.4a**) is limited by too strong reactivity, associated with the elementary processes of recombinative reactions, diffusion, and desorption. In contrast, the activity of catalysts/sites in the right leg(such as D and E in **Fig. 1.4b**) is limited by weak reactivity, resulting in a low coverage of reacting species and high barriers of dissociation[5, 20].

The scaling relation can be different due to the modification of local surface, like an oxygen vacancy, as shown in **Fig. 1.4c**. As a consequence, a new volcano plot (blue line in **Fig. 1.4d**) and reaction phase diagram can be achieved with improved activity. Oxygen defects of TiO_2 have been the focus of interest due to charges trapping and the formation of small polarons[35, 36, 37, 38]. Charge-trapping centers on defective surfaces are usually considered as favored sites for adsorption and chemical reactions[39, 40, 41]. Note that oxygen vacancies are not typically present on the anatase TiO_2(101) surface[40], but can be created by photo beam under illumination condition[40, 42].

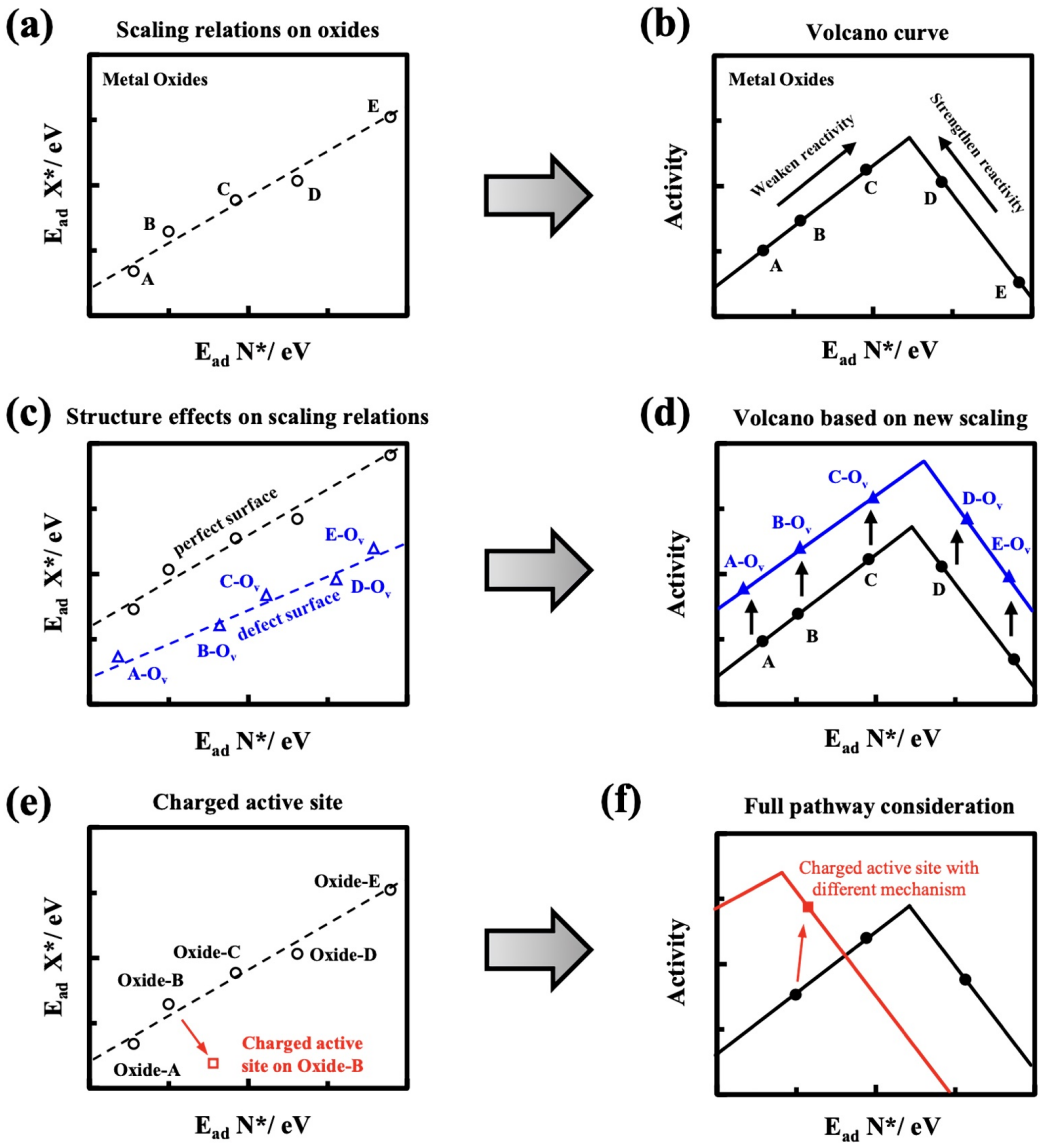

Fig. 1.4 Strategy for computational investigation of catalysis. (a) Schematic diagram of linear correlations between adsorption energies (scaling relation) over oxide surfaces. N* refers to the adsorbed N, which is the descriptor applied in the project, X* refers to other adsorbates. (b) Traditional activity volcano plot for oxides. (c) New linear correlations between adsorption energies caused by local effects (e.g. oxygen vacancy). (d) The improved volcano plot based on new scaling relations over local effects. (e) Breaking the scaling relation on a charged system in photocatalysis. (f) Activity trend with the consideration of different reaction mechanisms[5].

In addition, the activity of deNO$_x$ may be significantly different without and with illumination due to the effect of localized charge on the surface induced by the photo excitation, which may break the scaling relation of adsorption energies(**Fig. 1.4a, e**) and the volcano plot and shift the volcano plot to a higher activity.(**Fig. 1.4f**) The photogenerated charge may also give rise to a favored reaction pathway, which is different from the one under dark conditions[5, 7]. Therefore, unveiling the mechanism of pho-

tochemical deNO_x on TiO_2 surfaces is very important for improving catalyst design. In such a study, a full diversity of reaction pathways should be considered, but so far, only some hypothetical and simplified reaction pathways have been used to study photocatalysis over oxides[43]. The varying reaction mechanisms and pathways assumed in the literature have led to great uncertainties in the calculated activity for a new material. In principle, it is possible to develop a scheme with full consideration of all reaction pathways; however, the computational cost of the construction of extremely complex reaction networks is becoming a major challenge. Herein, I applied our recently developed new algorithm[5], which can efficiently consider the full set of pathways. Furthermore, this approach shows the basic influences that limit the efficiency and activity of the catalysts[5, 20].

The scaling reactions and volcano plots are based on calculated adsorption and reaction energies, as well as energy barriers, and the predictive power is critically dependent on the accuracy of these calculations. The results can be quite inaccurate if standard local or semilocal implementations of density functional theory (DFT) are used (because those have a strong tendency to charge delocalization)[44] or if the artifacts caused by the repetition of the charge in periodic models of charge-assisted processes (like photocatalysis) is not corrected[45]. Therefore, it is quite important to have a computational strategy based on:

1). An effective scheme of studying a full set of reaction pathways, for which our group have developed a new algorithm[5].

2). Accurate methods for calculating the energetics beyond standard density functional theory and charge corrections which our group have recently developed[46, 47, 48].

In this work, I used these aforementioned tools to address the highly important practical problem of increasing the activity of photocatalytic denoxification over oxides. I took into account a complete set of possible reaction pathways using a cutting-edge technology. Based on that, the calculated data obtained in a computational framework, which is capable to describe a huge number of charge-assisted reactions on oxide surfaces for the first time without the localization error of (as yet) standard electronic structure calculations, and completely free of the artifacts caused by imposing periodic boundary conditions on a charged system.

The thesis is organized as follows. I firstly introduce the fundamental principles of photocatalysis and the different crystalline phase of TiO_2 in Chapter 2, the computational methods and data analysis tools are discussed in Chapter 3, the computational parameters and models used to calculate the adsorption energy, to establish the reaction network, and to search for optimal reaction pathways are described in Chapter 4. The activity and selectivity maps of deNO_2 under dark and illumination conditions are given in Chapter 5. The activity and selectivity maps of deNO over diverse TiO_2 surfaces under dark and illumination conditions are given in Chapter 6. Microkinetic modelings of

photocatalytic deNO over titania surface and modified zeolite are given in Chapter 7. Finally, I present my conclusions and the insights obtained in this work as well as the implications for the photocatalysis field in general.

2 | Photocatalysis on titania

2.1 Basic principles in photocatalysis

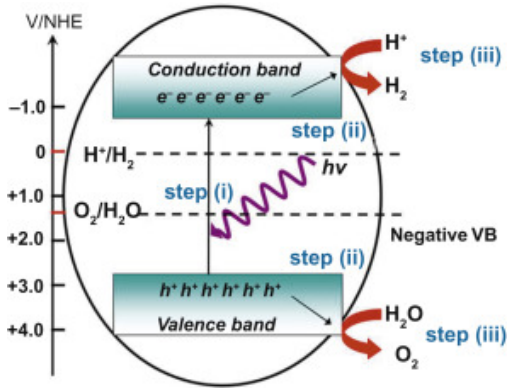

Fig. 2.1 The schematic mechanism of photocatalytic water splitting. Step (i): excitation, step (ii): charge migration, step (iii): surface catalysis[6].

Photocatalysis, like photoassisted chemical reactions on a solid surface, relies on charge carriers generated by photoexcitation[6, 7]. The semiconductor will be excited as the energy of photons is equal to or larger than its band gap, leading to the generation of free moving electron-hole pair in the conduction band and valence band of the semiconductor, respectively. Theoretically, the more photons semiconductors can absorb, the higher the achieved efficiency of the semiconductor-based system[6]. The next step is defined as the “charge migration” step. The photogenerated electron and hole pairs migrate to the surface of the semiconductor. Note that the recombination of the electron and hole pairs should be inhibited in this step. Because the charge recombination significantly decreases the amount of the available active charges for further photocatalytic reactions. Therefore, it is crucial to propose strategies that can promote charge separation and transportation. This can be generally realized by p-n junction, loading cocatalysts and so on.

The last step is defined as the "surface catalysis" step. The electron can facilitate chemical reduction reactions and the hole can facilitate chemical oxidation reactions on the surface. A schematic illustration of photocatalytic water splitting is depicted in **Fig 2.1**. After photoexcitation, the photogenerated electron and hole can be used to

reduce H^+ and oxidize H_2O, respectively. In principle, the bottom of the conduction band(CBM) must be higher than the H^+/H_2 reduction potential (0 V vs. NHE at pH = 0) and the top of the valence band(VBM) must be lower than the O_2/H_2O oxidation potential (1.23 V vs. NHE at pH = 0). Therefore, a semiconductor with a band gap greater than the thermodynamic requirement of 1.23 eV and straddling the redox potential of H_2O would be an appropriate candidate for water splitting[6].

2.2 Introduction to titania

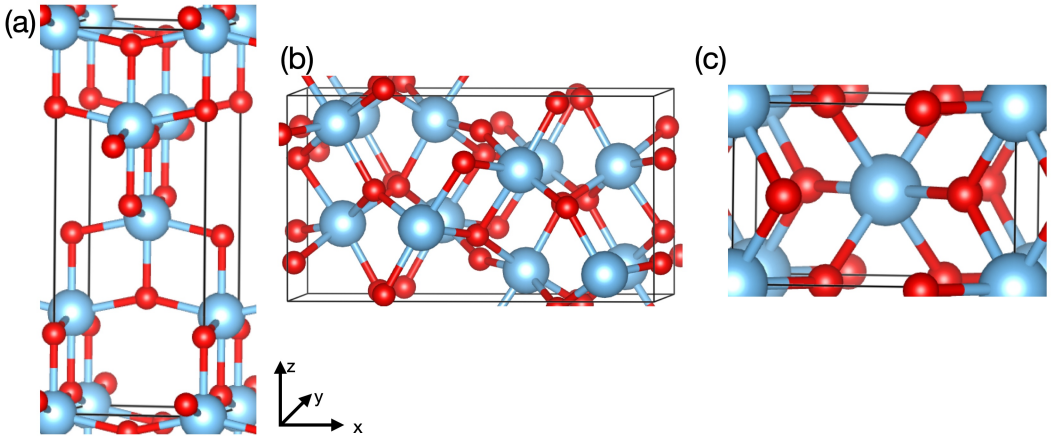

Fig. 2.2 Crystal structure of anatase (a), brookite(b) and rutile(c)

Titanium dioxide (TiO_2) is a low-cost, non-toxic, environmentally-friendly and simple-to-handle material. It has been widely investigated in photocatalysis since it was reported that TiO_2 could successfully decompose H_2O with irradiation by Fujishima and Honda in 1972[49]. TiO_2 has three major polymorphs: anatase, rutile, and brookite (**Fig. 2.2**) with band gap of 3.2 eV, 3.0 eV and 3.4 eV, respectively[50]. In all these TiO_2 phases, the Ti atom is six-fold coordinated and is surrounded by six O atoms, forming a octahedron, TiO_6[6]. The O atom is three-fold coordinated. The conduction band of TiO_2 mainly consists of Ti_{3d} orbitals and the valence band consists of O_{2p} orbitals. Rutile is the thermodynamically most stable phase, the other two forms of TiO_2 can convert to rutile when the heating temperature exceeds 600°C[18]. It is believed that anatase has a higher chemical activity than rutile[51]. Despite the fact that anatase is frequently noted as the most photo active polymorph, numerous studies report that rutile has comparable photo activities than anatase[3, 52]. Most commercial products of TiO_2 are mixtures of rutile and anatase, like Degussa P25 TiO_2, which is mixed by 25% rutile and 75% anatase. The mixed phase has been widely used in laboratory studies because it usually performs better than any of the individual phase[3, 53]. In principle, it is hard to compare the performance of different polymorphs of TiO_2 under illumination conditions since many factors can affect the photo activity of TiO_2, such

as the ratio of morphology, surface structure, and surface chemistry for different TiO_2 samples as well as the target reactions[3]. At present, it cannot be concluded that the activity of anatase and rutile are essentially different. It would be quite helpful in the choice of experiments if the activity and selectivity of photocatalytic denitrification on various titania surfaces was understood.

The most stable facet of anatase TiO_2 is the (101) surface that contributes around 94% of the exposed crystal surface[54]. The most stable facet of rutile TiO_2 is (110) surface[55]. As mentioned before, oxygen vacancies are regarded as important adsorption sites[56], and active centers for reactions[4, 57], like water splitting at an oxygen vacancy[55, 58]. In principle, removing a bridging oxygen atom from TiO_2 surfaces leads to the formation of two reduced Ti^{3+}[55], which make contributions to the donor levels in the electronic structure of TiO_2[59, 60]. Thus, much attention were paied to the development of synthesis of TiO_2 with oxygen vacancies and exploration of its unique properties for photocatalytic applications. Thus, I focused primarily on defective and perfect anatase(101) and rutile(110) surfaces in this work.

3 | Computational methods

3.1 Density functional theory

Electronic structure calculations are extremely important in computational material science since most of the properties of a system are determined by its electronic structure, i.e. the spatial and energy distribution of electrons[61]. In 1926, Erwin Schrödinger firstly published his now-famous wave equation, which appeared to be extremely promising because it contained all available information about a system[62]. The Schrödinger equation was further simplified by the Born-Oppenheimer(BO) approximation[63], which took advantage of the significant differences between the masses of nucleus and electrons, separating the motion of the fast moving electron from that of the slow heavy nucleus. However, the Schrödinger equation is still difficult to solve even under the BO approximation when the number of electrons is large, due to the complex interactions between electrons. The difficulty of solving the Schrödinger equation grows exponentially with the number of electrons. Notably, Paul Dirac in 1929 attributed this difficulty to the lack of mathematical theory in dealing with a large part of physics and the whole of chemistry[64]. Then, the Hartree-Fock(HF) approximation, was utilized to solve the complex many-electron wave function. The HF theory replaces the real electrons with fictitious non-interacting electrons (so called one-electrons), whose wave functions are determined in such a way that the Slater determinant[65], set up from them, mimics the real many-body wave function. In other words, it assumed that there is no direct interaction between electrons and these non-interacting electrons move in a mean field of the rest, without knowing where the others are, i.e., without correlation between their motions. The total wave function can be expressed as a Slater determinant of N spin-orbitals to fulfill the Pauli-exclusion principle[65, 66, 67]. The disadvantages of HF methods are that it didn't cover the electron correlation and the computational cost is proportional to the 4th power of the number of electrons. Thus, it was desired to find a new method, which has to be rigorous but able to minimize the computational complexity as much as possible. Then, the density functional theory(DFT) was born.

In 1964, Hohenberg and Kohn published a landmark paper[68] and the theorems proven in this report are the bedrock for all modern density functional theories. The Hohenberg-Kohn theorems concerns any system consisting of electrons moving under

the influence of an external potential ($V_{ext}(\mathbf{r})$)[68]. The first HK theorem demonstrates that the ground-state properties of a many-electron system are uniquely determined by an electron density that depends on only three spatial coordinates. Namely, the ground-state wave function and the all other properties of the system defined by an external potential(V_{ext}) are determined by the ground state density.

In second theorem, they defined a universally valid functional, F[ρ]:

$$F[\rho] = T[\rho] + E_{ee}[\rho] \tag{3.1}$$

$$E[\rho] = \int \rho(r) V_{ext} dr + F[\rho]. \tag{3.2}$$

This functional reaches its minimum value if and only if the input density is the true ground state density. All the theorems tell us is that there is a unique mapping between the ground state density $\rho_0(\mathbf{r})$ and the ground state energy E_0.

Unfortunately, the exact construction of F[ρ] is unknown. In 1965, Kohn and Sham made a significant breakthrough and they introduced the concept of a non-interacting reference system built from a set of orbitals (i. e., one electron functions) such that the major part of the kinetic energy can be computed to good accuracy[69]. The kinetic energy can be written as:

$$T_s = -\frac{1}{2} \sum_{i}^{N} < \phi_i | \nabla^2 | \phi_i > \tag{3.3}$$

,where ϕ_i is called Kohn-Sham orbitals, or briefly KS orbitals. The energy functional of the true system can be written as:

$$\begin{aligned} E[\rho(\overrightarrow{r})] &= T_S[\rho] + J[\rho] + E_{\text{xc}}[\rho] + E_{\text{ext}}[\rho] \\ &= T_S[\rho] + J[\rho] + E_{\text{xc}}[\rho] + \int \rho(r) V_{\text{ext}} dr \end{aligned} \tag{3.4}$$

,where J[ρ] is Coulomb interaction and J[ρ] = $\frac{1}{2} \int \int \frac{\rho(r)\rho(r')}{|r-r'|} dr dr'$, $E_{\text{xc}}[\rho]$ is exchange correlation energy and $E_{\text{xc}}[\rho] \equiv (T[\rho] - T_s[\rho]) + E_{ee}[\rho] - J[\rho])$. The exchange-correlation energy is also the functional of density and it contains everything that is unknown and also the the difference between the true kinetic energy and that of Eq.(3.3). The Kohn-Sham energy expression is subjected to the variation principle with respect to independent variations in the orbitals:

$$[-\frac{1}{2}\nabla^2 + V_{\text{ext}}(r) + V_{\text{coul}}(r) + V_{\text{xc}}(r)]\phi_i(r) = \epsilon_i \phi_i(r) \tag{3.5}$$

By this method, once we know the V_{xc}, the Kohn-Sham orbital can be obtained by solving the Kohn-Sham equation by the self-consistent field method. However, the

exchange-correlation energy can not be exactly calculated and approximations for exchange correlation functional must be used. Therefore, the main goal of modern density functional theory is to find better approximations for exchange correlation energy and the quality of the density functional approach depends entirely on the accuracy of the selected approximation to E_{XC}[70]. The main developed approximations are the local density approximation (LDA)[71], meta-GGA, general gradient approximation (GGA)[72], hybrid functional[73]("Perdew's ladder"). LDA can produce good structural properties but fails to produce binding energies due to overbinding[61]. GGA can provide reasonably accurate results within absolute average errors of about 5 kcal/mol for at atomization energies[61] but it usually causes delocalization errors and underestimation of the band gap in semiconductors and insulators. Hybrid functionals incorporate some Hartree-Fock exchange (HF) and are semi-empirical in nature[74]. Hybird functionals successfully provide the best performance in many applications but they are costly[61].

3.2 Lany-Zunger correction on GGA functional

As mentioned above, the inaccuracy of the standard local and semi-local approximations (LDA and GGA, respectively) leads to several problems, such as the underestimation of the band gap and delocalization of electron states. Thus, they are unable to describe small polarons (charge trapped in a strongly localized state by distortion of the pristine lattice)[75]. This problem can be avoided by using the hybrid exchange functional(HSE)[76, 36, 77], which can reproduce the band gap and fulfill the generalized Koopman's theorem (gKT)[78]. The gKT is a requisite for proper localization of states, predicting correct ionization energies[78, 79]. However, it is costly to simulate surface reactions with a HSE functional. GGA-LZ functional, a GGA functional with corrections introduced by Lany and Zunger, provides possibilities to the investigation of a complex reaction network. The band gap is corrected by using non-local external potentials[78], and occupation-dependent localizing potentials make sure that the gKT is satisfied. However, it was found that the localization potentials, with parameters determined for the bulk, do not satisfy the gKT for states localized on the surface, due to changes in the electronic screening. Thus, for properly treating surfaces, Meisam and co-workers have extended the Lany-Zunger (LZ) method by introducing coordination-dependent parameters for the localizing potentials[46]. This method can correctly predict charge localization both in the bulk and on the surface, and provides a good approximation of the much more expensive HSE results.

As shown in **Figure 3.1a and 3.1c**, a pure PBE(Perdew-Burke-Ernzerhof) calculation leads to the complete delocalization of an excess electron and hole over the entire bulk of the slab, whereas PBE + LZ describes the small polaron state well. A localized

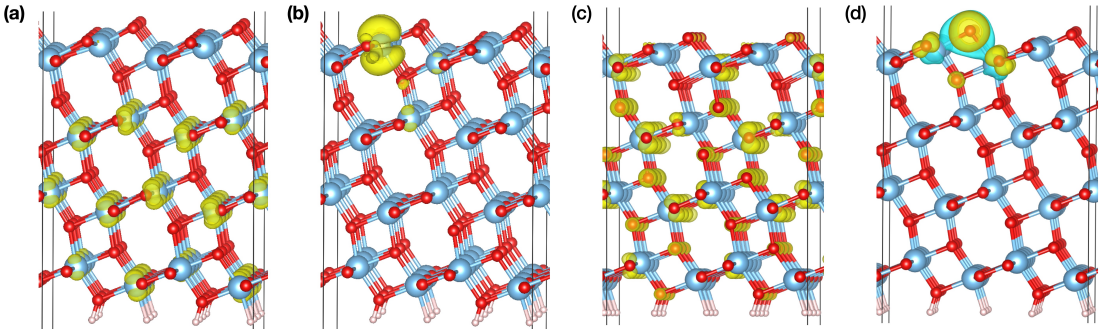

Fig. 3.1 The effect of the LZ-correction. Distribution of an extra electron in a pristine TiO_2(101) slab, as obtained from GGA without (a) and with (b) the Lany-Zunger correction. Distribution of an extra hole in a pristine TiO_2(101) slab, as obtained from GGA without (c) and with (d) the Lany-Zunger correction.The two spin directions are distinguished by color. Cyan, red, and pink denote Ti, O, and H, respectively.

electron state around a single Ti atom with strongly relaxed environment is shown in **Figure 3.1b** and a localized hole state around bridging O atom with relaxed environment is shown in **Figure 3.1d**. These results are consistent with higher level (HSE06) calculations by us and others[75, 76, 80]. This is an important improvement and the basis for analyzing charge-assisted photocatalytic reactions. The PBE(Perdew-Burke-Ernzerhof) + LZ calculation also reproduces the results for the neutral vacancy, as obtained by HSE06[81] and by screened exact exchange functional (sX) calculations[82]. It is obvious, that this has a profound effect on charge assisted surface reactions. Note that the delocalization tendency of plain GGA does affect the energetics of reactions in the dark too, if they are involving defects or adsorbates which give rise to levels in the band gap of TiO_2. HSE calculations in modelling heterogeneous catalysis are scarce and limited in scope. I applied GGA + LZ here for large scale calculations, with occasional checks using HSE.

3.3 Modeling charge assisted surface reactions

Herein, I used static electronic structure calculations in a model with a net charge to simulate the oxidation and reduction reactions, respectively. The net charge induces severe problems. For that reason, general computational studies of photocatalysis usually do not consider the effect of charge on the surface at all[80, 83, 84, 85], except when either a species with opposite charge is assumed in the gas phase[82] or a non-periodic model is used[86].

Adding a localized charge to a periodic model leads to an infinite Coulomb-energy, due to the electrostatic interaction between the periodic images[87]. To avoid that, in all electronic structure codes used for modelling periodic systems with a net charge, an evenly distributed (so called jellium) countercharge is added, to keep the repeated

supercell electrically neutral. Considering the different localization of the charge and countercharge, however, the repeated charges cause a spurious electrostatic potential, which affects the energy of the calculated one-electron states and shifts the total energy. For example, the formation energy of a charged Cl vacancy diverges with vacuum size and lateral size[87]. A posteriori method based on classical electrostatics was applied to correct bulk calculations with a charge[79, 88, 89, 90], but the correct treatment of a charge in the proximity of an interface is problematic because of the dielectric profile[87]. Our group recently have developed two procedures for charge corrections: SLABCC and SCPC. SLABCC calculates an a posteriori energy correction for charged slab models under 3D periodic boundary condition (PBC) based on the method of Komsa and Pasquarello[87], as implemented in the SLABCC code[47]. SCPC involves a potential correction, which automatically corrects both the total and the one-electron energies, as well as the wave functions, self-consistently and can be applied both in the bulk and for slabs. It has been implemented into the QE (Quantum Espresso) and VASP (Vienna ab initio simulation package) codes, two of the most commonly used electronic structure packages[48].

In this work, I employed these two charge correction methods and it was found that the new self-consistent potential correction (SCPC) method[48] have total energy corrections very close to the SLABCC results as shown in **Table A.1**.

3.4 Reaction phase graph method

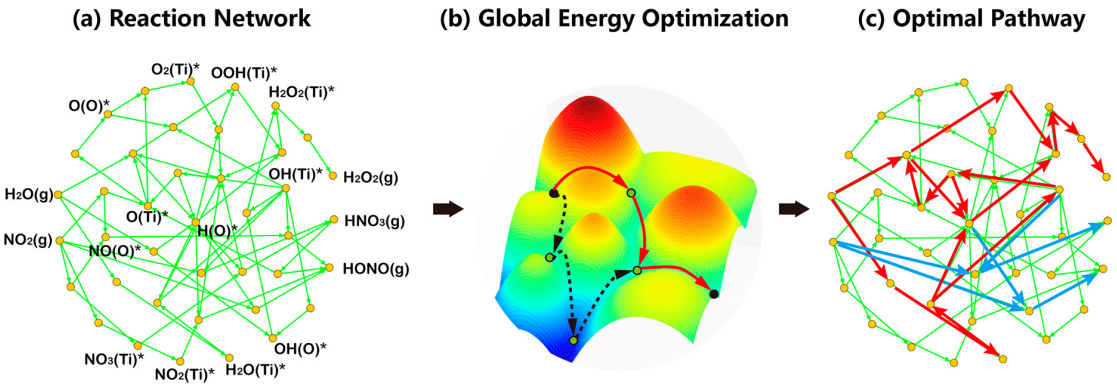

Fig. 3.2 (a) The complete deNO_2 reaction network with stable intermediates marked and transition states unmarked. (b) The algorithm of determining the pathways from global energy optimization, as described in Eq. 3.9. (c) The optimal reaction pathway for deNO_2 over the perfect anatase TiO_2(101) surface (blue, NO_2 evolutional paths; red, H_2O evolutional paths)[7].

To construct a full reaction network(**Figure 3.2**), the (m × n) stoichiometric matrix, S, describing all elementary steps and species, was established. The rows and columns in S (Eq. 3.7) correspond to the substances(m) and the elementary steps(n) of the con-

sidered reactions, respectively. An elementary step j is described by the chemical vector,

$$R_j = (v_{1j}, v_{2j}, v_{3j}, ..., v_{mj})^T \tag{3.6}$$

where v_j represents the stoichiometric number of the involved substances (reactants, intermediates, and products) in the relevant steps, and m represents substances in the reaction. T is the rank conversion of the matrix. Then, all possible pathways can be enumerated with free linear combinations of elementary step vector and the overall matrix S can be established as below[5]:

$$S = \begin{bmatrix} v_{1,1} & \dots & v_{1,m} \\ \vdots & \ddots & \vdots \\ v_{n,1} & \dots & v_{n,m} \end{bmatrix} \tag{3.7}$$

To speed up the computation, an accelerator strategy was developed. Two steps are performed prior to the enumeration of the combinations[5]:
(1) The intermediates (substances m, excluding reactants and products), which are only considered in one elementary step, are eliminated. (Elementary steps elimination)
(2) The elementary steps involved same intermediates B can be linked and pre-combined (e.g. A $\rightarrow$ B and B $\rightarrow$ C, where intermediate B only involves in these two reactions can be connected as A $\rightarrow$ B $\rightarrow$ C). (Precombination). The full enumeration can then be done, following:

$$c_i = [\alpha_1, \alpha_2, \dots, \alpha_n], \alpha \in [1 \dots n] \tag{3.8}$$

where c_i and α_n refer to a subset of elementary steps and to the chemical vector of the involved substances in the newly combined relevant steps, respectively.

A rank-based method were used to determine whether the individual combination leads to a possible pathway[5, 7]. The ΔG_{RPD}-limiting steps are the reaction determining steps, which can be deduced from the reaction phase diagram (RPD) analysis as shown in **Figure 3.2b, c**. In principle, the optimal reaction pathway is the one with the minimal free energy change in the limiting step at a given site. Thus, the descriptor value (x) could be identified using the following equation:

$$\Delta G_{RPD}(x) = min_i(max_j(\Delta G_{(i,j)}(x)) \tag{3.9}$$

where i denotes the possible reaction free energies, which were obtained using all forward and backward elementary steps. All possible reaction pathways were obtained by the free combination of all the considered elementary steps. j denotes the elementary step with the maximum ΔG_{RPD} (ΔG_{RPD}-limiting step) in each pathway, which was selected and compared with all other pathways to minimize the ΔG_{RPD}-limiting ener-

gies for total considered reactions. For instance, the pathways A and B consist of (R1 + R2 + R3 + R4) and (R5 + R6 + R7 + R8), respectively. R2 and R5 are most unfavorable over all elementary steps in internal comparison for the pathways A and B, respectively, while R5 is more favorable with respect to R2. As a result, pathway B is defined as the optimized reaction channel and R5 is the ΔG_{RPD}-limiting step. Herein, the ΔG_{RPD}-limiting energies over all active sites were used to determine the (quasi) activity trend and mechanism variation under dark and illumination conditions[7].

3.5 Microkinetic simulations

Microkinectic modeling has been widely applied in complex reaction mechanisms in last few decades[43, 91, 92]. It plays an important role in understanding the activity and selectivity of catalysts and in catalyst design[43]. Because it is possible to quantify the importance of not only each elementary step, but also each intermediate and transition state in the reaction mechanism by a general concept degree of rate control(DRC)[93, 94]. The definition of DRC[93] is :

$$X_i = (\frac{\delta(lnr)}{\delta(-G_i^0/RT)}) \tag{3.10}$$

or

$$X_i = \frac{\delta(lnr)}{\delta g_i} \tag{3.11}$$

$$g_i = -G_i^0/RT \tag{3.12}$$

, where r is the net steady-state rate for consumption of one reactant. G_i^0 is the standard-state Gibbs free energy of species i.

A microkinetic simulation can be performed by the following steps:

- Proposing a reaction mechanism.
- Calculating all the reaction energies and reaction energy barriers.
- Using CATKINAS package[95] to simulate the reaction with practical industrial or experimental catalytic conditions.
- Finally, the CATKINAS package outputs the results including activity, coverage, reversibility, sensitivity, energy profile and reaction flow diagrams.

3.6 Calculation of adsorption energy

In the deNO$_2$ process, the adsorption energies of the relevant intermediates on the solid surface, with respect to the gas phase energies of NO_2, H_2O_2 and H_2O, were obtained from the following equation:

$$E_{\mathbf{ads}} = E_{\mathbf{tot}} - E_{\mathbf{sur}} - (\mathbf{x}\mathbf{E}_{\mathbf{H}} + \mathbf{y}\mathbf{E}_{\mathbf{O}} + \mathbf{z}\mathbf{E}_{\mathbf{N}}) \tag{3.13}$$

, where x, y and z denote the number of H, O and N atoms, respectively.

In the deNO process, the adsorption energies of relevant intermediates on the solid surface referred to the gas phase energies of NO and O_2, which were obtained from the following equation:

$$E_{\mathbf{ads}} = E_{\mathbf{tot}} - E_{\mathbf{sur}} - (\mathbf{x}E_{\mathbf{O}} + \mathbf{y}E_{\mathbf{N}}) \tag{3.14}$$

, where x and y denote the number of O and N atoms, respectively.

The thermal correction for Gibbs free energy(G) includes the zero point energy(ZPE) and Gibbs free energy difference between 0 K and T K, i.e., the correction for G(T) = ϵ_{ZPE}+ $\Delta G_{0\rightarrow T}$. The thermal corrections were obtained using the methods implemented in VASPKIT program[96]. The temperature (T) and pressure (P) were set according to the relevant experimental conditions. In the deNO$_2$ process, T = 298K, P = 202.65 nbar, 9.12 nbar, 2.53 nbar, 9.12 nbar and 3.04 nbar, for NO_2, H_2O, H_2O_2, HONO, and HNO_3 respectively[97]. In the deNO process, T = 493K, P = 1.0E-6 atm for NO[4]. The climbing image nudged elastic band (CI-NEB) method[98, 99, 100] and dimer method[101] were applied to search for transition states (TSs). The TSs were confirmed by frequency calculations to have only one imaginary frequency.

4 | Computational setup

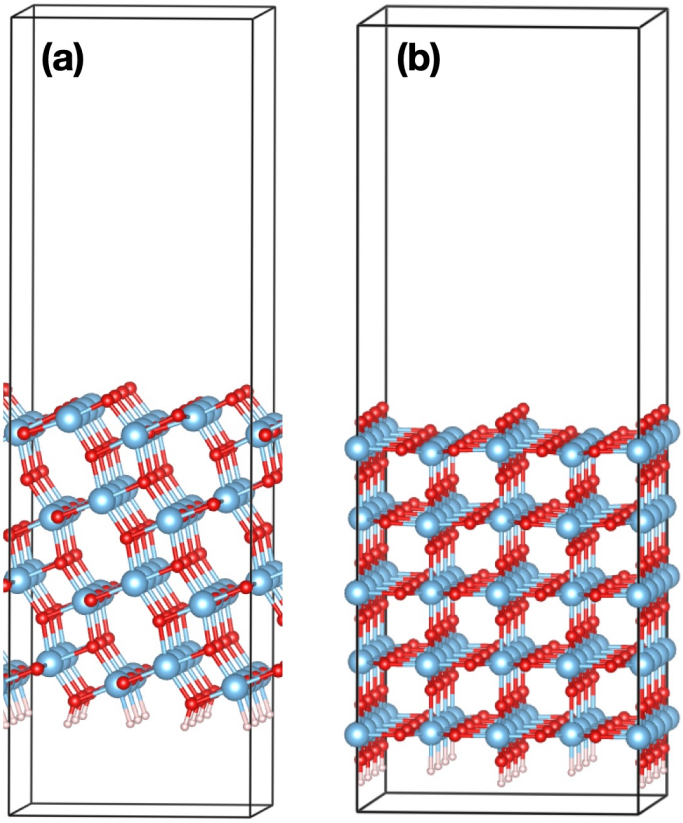

Fig. 4.1 (a) The relaxed structures of the anatase(101) (a), and rutile(110) (b) slabs. Cyan, red, and pink denote Ti, O, and H, respectively.

The lattice parameters a = 3.741 Å and c = 9.526 Å for anatase and a = 4.571 Å and c = 2.960 Å for rutile were used. The anatase (101) surface was modeled by a slab of four bi-layers with a 3×1 surface supercell. The rutile (110) surface was modeled by a slab of five layers with a 4×2 surface supercell. A vacuum layer of 20 Å was applied. The two bottom layers were fixed and the five-fold coordinated Ti ($Ti_{\mathbf{5c}}$) and two-fold coordinated O ($O_{\mathbf{2c}}$) atoms were saturated by $H^{\mathbf{1.33}}$ and $H^{\mathbf{0.66}}$ pseudo-hydrogen atoms, respectively to avoid surface state. The optimized slab models are shown in **Figure 4.1**. All optimized adsorption geometries are shown in **Appendix B, C**. The valence electrons($10e^-$ for Ti and $6e^-$ for O) were treated by plane

wave based GGA calculations, using the PBE exchange correlation functional[102]. The core-electrons were treated using the projector augmented wave method implemented in the VASP package[103, 104, 105]. A cutoff of 420 eV was used for the plane wave expansion and a cutoff of 840 eV was used for the charge density representation in the real space grid. GGA + U were applied in calculations of zeolite clusters with the U value for Ti 4.20 eV[106]. Lany-Zunger corrections were applied in calculations on the TiO_2 surface to reproduce the band gap and localize the polarons in an efficient way[78, 79]. SLABCC[47] and SCPC[48] methods were applied to correct the total energies in charged system as shown in **Appendix A**.

5 | Activity and reaction mechanism mapping of photocatalytic deNO$_2$ processes on anatase TiO$_2$(101) surface

As we known that NO_2 is more toxic than NO, it heavily affects the overall deNO$_x$ processes[14]. Thus, NO_2 conversion on TiO_2 was focused on firstly. In experiments, various techniques have been applied to study NO_2 adsorption on TiO_2 particles and surfaces such as fourier transform infrared (FTIR) spectroscopy and XPS[12, 107]. It was reported that HONO and HNO_3 was produced on TiO_2 via the reaction of H_2O and NO_2 under dark conditions[97, 107, 108, 109]. It might be also noted that HONO is an important source of reactive $OH^\bullet$ radicals and key oxidant in the degradation of most air pollutant in the troposphere, which makes HONO formation reaction attach great attention[11]. The reaction mechanism of dark condition has been widely discussed in published papers but it's still controversial[110, 111, 112, 113, 114]. It was proposed that NO_2 disproportionation on TiO_2 has led to the formation of NO^+ and NO_3^-, where the formed anion and cation can immediately react with H_2O to produce HONO and HNO_3 in the subsequent steps[111, 110, 112, 113]. Haubrich et al have observed N_2O_4 at higher NO_2 pressure by XPS[12]. Furthermore, they suggested HNO_3 is formed by physisorbed NO_2 rather than chemisorbed NO_2 and NO_3 species[12]. However, Lambert suggested that HONO was formed by direct hydrogenation of NO_2 under dark condition, where the hydrogen was generated from water dissociation[97]. It was detected that both oxygen atoms in the product of HONO can stem from NO_2 rather than water by isotope-labelling experiments. This suggested that the observed N_2O_4 cannot be accounted for NO_2 hydrolysis under realistic pressures.

The photocatalytic mechanism is also disputed. Under UV illumination condition, it was reported by Lambert's group that H_2O_2 is a minor product and they proposed H_2O_2 was formed by the combination of OH radicals, arising from photocatalytic water splitting. Meanwhile, NO_2 captured the photogenerated electron and combined with H^+

to produce HONO[97]. However, Bedjanian and co-workers reported the main product was HONO with illumination and they didn't detect H_2O_2[109]. Therefore, deNO$_2$ with the presence of water on TiO_2 surface is complex and not yet clearly understood and further studies are needed to understand them.

(R0) $H_2O(g) + * \rightarrow H_2O(Ti)*$
(R1) $H_2O(Ti)* + * \rightarrow H(O)* + OH(Ti)*$
(R2) $OH(Ti)* + * \rightarrow H(O)* + O(Ti)*$
(R3) $* + NO_2(Ti)* \rightarrow O(Ti)* + NO(Ti)*$
(R4) $* + NO_2(g) \rightarrow NO_2(Ti)*$
(R5) $H(O)* + NO_2(Ti)* \rightarrow 2* + HONO(g)$
(R6) $H(O)* + NO_2(g) \rightarrow * + HONO(g)$
(R7) $OH(Ti)* + NO_2(g) \rightarrow * + HNO_3(g)$
(R8) $2NO_2(g) + 2* \rightarrow NO(O)* + NO_3\ (Ti)*$
(R9) $NO(O)* + OH\ (Ti)* \rightarrow HONO(g) + 2*$
(R10) $H(O)* + NO_3(Ti)* \rightarrow HNO_3(g) + 2*$
(R11) $HNO_3(g) + * \rightarrow O(Ti)* + HONO(g)$
(R12) $OH(Ti)* \rightarrow OH(O)*$
(R13) $H_2O(g) + 2* \rightarrow H(O)* + OH(O)*$
(R14) $OH(O)* + OH(Ti)* \rightarrow * + H_2O_2(Ti)*$
(R15) $O(Ti)* \rightarrow O(O)*$
(R16) $O(O)* + O(Ti)* \rightarrow * + O_2(Ti)*$
(R17) $O_2(Ti)* + H(O)* \rightarrow * + OOH(Ti)*$
(R18) $O(O)* + OH(Ti)* \rightarrow * + OOH(Ti)*$
(R19) $H_2O(g) + O(Ti)* \rightarrow H(O)* + OOH(Ti)*$
(R20) $OOH(Ti)* + H(O)* \rightarrow * + H_2O_2(Ti)*$
(R21) $H_2O_2(Ti)* \rightarrow * + H_2O_2(g)$

Table 5.1 The considered elementary steps for the deNO$_2$ reactions on anatase TiO$_2$(101) surface.

To simplified the reaction network, 22 possible elementary steps were considered in the deNO$_2$ reaction network as listed in **Table 5.1**. I obtained a total of 529 possible reaction pathways via the free combination of the all forward and backward elementary steps, and the complete reaction network is shown in **Fig. 3.2**. In the preliminary work, I also considered the combination of two species that are both adsorbed to Ti sites and other migration steps. However, due to the higher thermodynamic energy barriers, these elementary steps are not included in the optimal reaction pathways, so I have removed them in the following work. The adsorption energies of all important intermediates (H*, O*, NO_2*, OH*, OOH*, NO*, NO_3*) and adsorbed molecules (H_2O*, H_2O_2*) were calculated for different active sites on the surface of defective and perfect anatase TiO$_2$(101). There are five considered active sites, such as oxygen vacancy(Vo), four-fold coordinated Ti ($Ti_{\mathbf{4c}}^{\mathbf{defect}}$), five-fold coordinated Ti of defective surface ($Ti_{\mathbf{5c}}^{\mathbf{defect}}$), five-fold coordinated Ti of perfect surface ($Ti_{\mathbf{5c}}^{\mathbf{perfect}}$) and bridging oxygen($O_{\mathbf{br}}$). To estimate the reaction free energies and improve the accuracy, two-dimensional fitting

was applied to establish the correlations between the adsorption free energies and the descriptors. The adsorption energies of N(Ti)* and OH(Ti)* were chosen as descriptors for the adsorption energies of all reaction species. As shown in **Fig. 5.1**, the descriptor for the adsorption free energy of NO*, H_2O_2*, NO_2*, NO_3*, O_2* and H_2O* was G_{ad} N(Ti)* and the descriptor for adsorption free energy of OOH*, O*, OH* was G_{ad} OH(Ti)*. The scaling relations show good linearity. Note that the adsorption free energies of the bridging oxygen sites on perfect and defective surfaces of the considered species are considered to be the same, since the calculated energies were quite close. Based on the scaling relations, the free energy change of each elementary step can be described by descriptors.

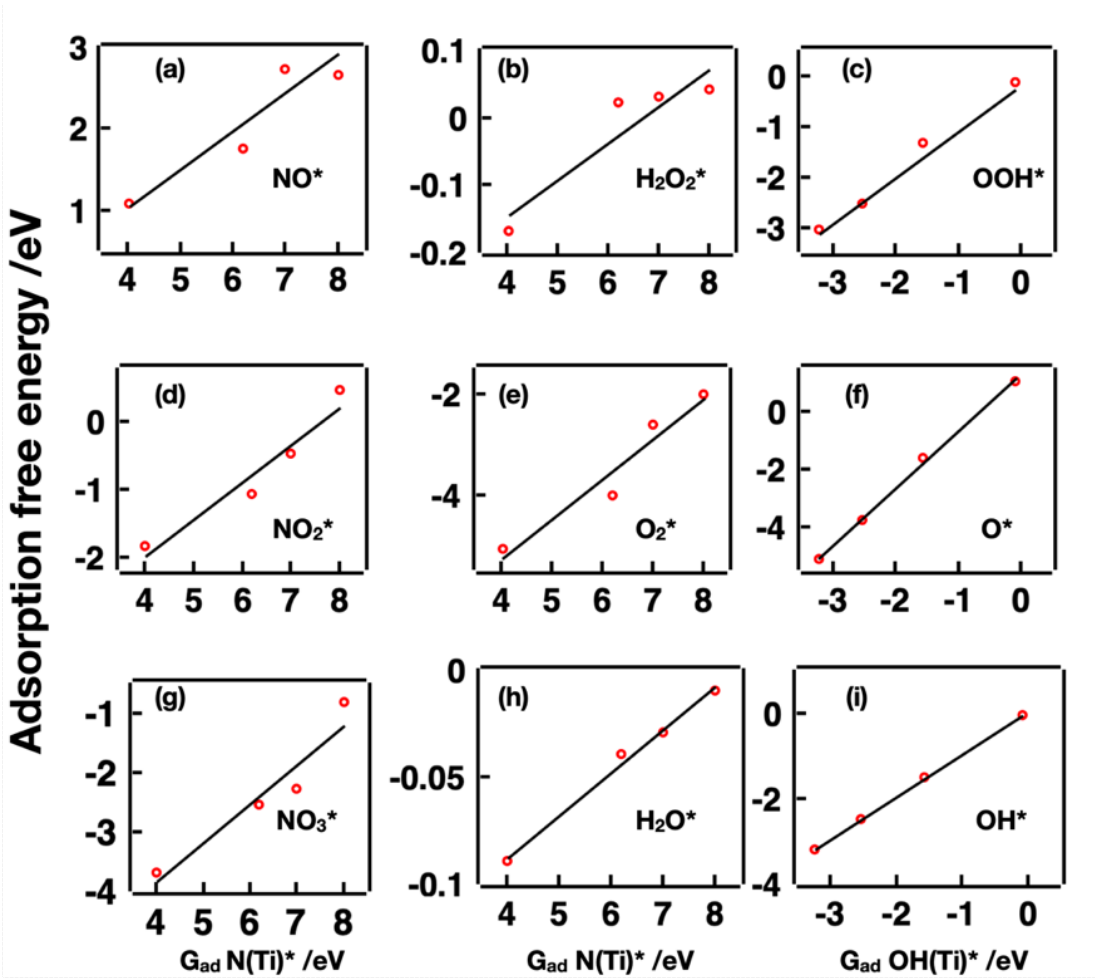

Fig. 5.1 Scaling relations of the adsorption free energies for (a) NO*, (b) H_2O_2*, (c) OOH*, (d) NO_2*, (e) O_2*, (f) O*, (g) NO_3*, (h) H_2O*, (i) OH* of different active sites on the perfect and defective anatase TiO_2(101) surface. All the adsorption energies were calculated with reference to the energy of the gas molecules NO_2, H_2O_2 and H_2O. The adsorption free energies of N(Ti)* and OH(Ti)* were chosen as descriptors.

5.1 Activity and mechanism mapping of NO_2 and H_2O without illumination on anatase TiO_2(101) surface

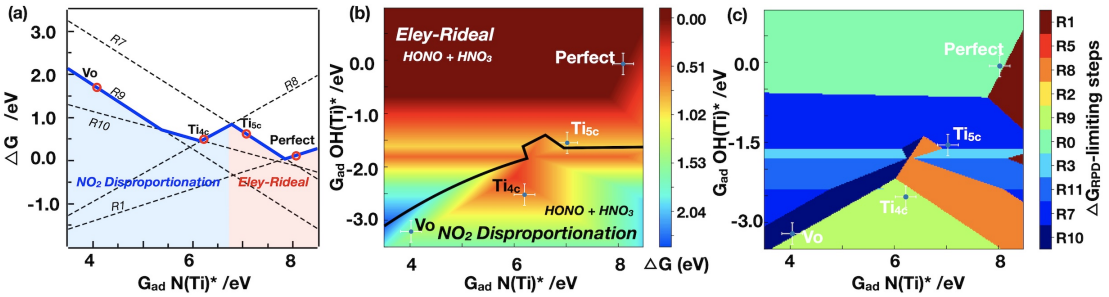

Fig. 5.2 (a) The reaction free energies of key elementary steps on all sites without illumination. Based on the scaling relationships between the adsorption free energies of adsorbates and descriptor (G_{ad} N(Ti)*), the reaction free energies (ΔG) can be described by the descriptor (G_{ad} N(Ti)*). The bold blue line denotes the 1D ΔG_{RPD}-limiting steps for NO_2 + H_2O reactions on different sites, which are determined with Eq. 3.9. "NO_2 disproportionation" and "Eley-Rideal" denote that the favored pathways follow NO_2 disproportionation and Eley-Rideal mechanisms, respectively. (b) The 2D (quasi) activity map without illumination is shown with two descriptors: adsorption free energies of N(Ti)* and OH(Ti)*, independently. The color bar denotes the limiting reaction free energies. (c) The 2D ΔG_{RPD}-limiting steps for the NO_2 + H_2O reactions on different sites without illumination. Vo denotes the oxygen vacancy; Ti_{4c} and Ti_{5c} denote the 4-fold and 5-fold coordinated Ti site on the defective surface, respectively. "Perfect" denotes the 5-fold coordinated Ti site on the perfect surface. The corresponding elementary steps are listed in **Table 5.1**

As shown in **Fig. 5.2a, b**, it was found that all sites were selective to HONO + HNO_3 production under dark conditions, which is in agreement with the experimental report [97], while the perfect surface exhibits the highest activity. Water dissociation on defective surfaces was thermodynamically favored, as shown in **Fig. 5.2a**. This is consistent with previous reports that water dissociation required a lower barrier on the reduced anatase TiO_2(101) surface[39, 41]. On the defective surface, the deNO$_2$ activity on Ti_{5c} and Ti_{4c} is relatively better than on Vo with the ΔG_{RPD}-limiting energies of 0.87 eV and 0.69 eV, respectively. As shown in **Fig. 5.2c**, the main ΔG_{RPD}-limiting steps are:

(R7) OH(Ti)* + NO_2(g) → HNO_3(g)

and

(R9) OH(Ti)* + NO(O)* → HONO(g) + 2*

On the defective surface, the OH* species has a too strong interaction with the defective surface sites, which hinders recombinative desorption. (Note that the labeling of the reactions follows that of **Table 5.1**.) Therefore, the defective surface, especially the Vo site, exhibits strong reactivity but low catalytic activity for deNO$_2$ reactions. On the perfect surface, the ΔG_{RPD}-limiting step is water adsorption. In general, there

are multiple activity optima because of the diverse reaction pathways. The optimal reaction pathways to produce HONO and HNO_3 were identical on the Ti_{5c} site of the defective surface and the perfect surface. HONO was formed by the combination of H* and NO_2(g), while HNO_3 was produced by OH(Ti)* + NO_2(g) $\rightarrow$ HNO_3(g) + * via the Eley-Rideal mechanism. This is consistent with Habrich's observation on the rutile TiO_2(110) surface[115, 116]. Namely, the HNO_3 production required weakly adsorbed NO_2 species[115]. Note that the strong adsorption energy of OH(Ti)* inhibits the recombinative desorption (R9 and R7), which is adverse for the deNO$_2$ activity. On Ti_{4c} and Vo sites, HONO and HNO_3 were produced via the disproportionation of NO_2 (R8), where the generated NO(O)* and NO_3(Ti)* species reacted with the dissociated water to produce HONO and HNO_3. Note that some sites are located at the boundary of multiple elementary steps and pathways (**Fig. 5.2b, c**), which indicates that those elementary steps and pathways exhibit similar reaction activities. In other words, it is possible to produce HONO and HNO_3 via the disproportionation of NO_2 on the Ti_{5c} site, which is also the ΔG_{RPD}-limiting step with a reaction free energy of 1.01 eV.

5.2 Activity and mechanism mapping of NO_2 and H_2O with illumination on anatase TiO_2(101) surface

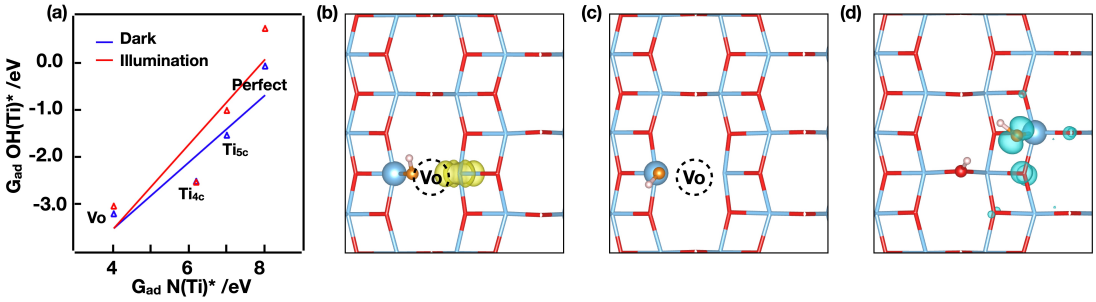

Fig. 5.3 (a) The correlation between G_{ad} N(Ti)* and G_{ad} OH(Ti)* under dark and illumination conditions. Spin density of OH* on (b) the neutral anatase TiO_2(101) slab with oxygen vacancy and (c) on the positively charged one. (d) Spin density of dissociated water adsorbed on perfect anatase TiO_2(101) slab with a positive charge. Yellow and turquois indicate positive (spin up) and negative (spin down) values, respectively. Cyan and red denote Ti and O of TiO_2(101), respectively. Orange and pink denote the O and H of OH*, respectively.

The combination of elementary steps (possible pathways) is a pure mathematical solution, which can not be different for illumination conditions. However, the most favorable pathway is indeed possible upon switching to another. With our algorithm, all possible pathways are determined prior to energetic comparison. It is feasible to reanalyze the most favorable pathway under illumination condition. The photogenerated charges can influence a given reaction pathway in multiple times, namely, multiple

photon processes. As the limiting step in dark conditions is the most important, I studied the effect only on the limiting step by a single photogenerated charge. As OH(Ti)* is a key species under dark conditions, I examined the G_{ad} OH(Ti)* in the presence of a photogenerated hole. At the Ti_{4c} and Vo sites, G_{ad} OH(Ti)* does not change, as shown in **Fig. 5.3a**. However, it is significantly weakened on the Ti_{5c} site of the perfect surface and on the Ti_{5c} site of the defective surface, and this has a crucial role in enhancing deNO$_2$ activity. As can be seen from **Fig. 5.3c**, the photogenerated hole on the defective surface is trapped by the reduced Ti, against our expectation, rather than on the OH(Ti)* (negative), so the G_{ad} OH(Ti)* remains intact. On the perfect surface, the hole is trapped by the OH(Ti)* (negative), giving rise to an OH radical, as shown in **Fig. 5.3d**. Therefore, the illumination has no significant effect on the activity of the Vo and Ti_{4c} sites, because the ΔG_{RPD}-limiting energies can not be lowered. However, the activity on the perfect surface can be enhanced.

Assuming that water adsorption is not directly affected by illumination, its dissociation was considered as a stepwise reaction[117]: deprotonation first and then oxidation: OH(Ti)* + hole $\rightarrow$ Pos-OH(Ti)* (R22) while the photogenerated electron was trapped by the proton. The adsorption free energies of OH(Ti)*, calculated on the positively charged surfaces (named as Pos-OH(Ti)*), and the adsorption free energy of N(Ti)* were chosen as descriptors. The reaction phase diagrams were established as shown in **Fig. 5.4a, b**, to analyze the deNO$_2$ activity in the photoassisted process. The perfect surface still exhibits the highest activity, and the limiting step is the same as under dark conditions. On the defective surface, the deNO$_2$ activity is enhanced on the Ti_{5c} site and the ΔG_{RPD}-limiting step has also changed, as shown in **Fig. 5.4c**. However, the Vo site remained inactive because of the too strong bonding interaction for Pos-OH(Ti)* species, which is consistent with our hypothesis above. The main production pathways of HONO and HNO_3 on all sites was unaffected by illumination. At Ti_{5c}, HONO and HNO_3 still prefer to be produced via H(O)* + NO_2(g) $\rightarrow$ * + HONO(g) (R6) and OH(Ti)* + NO_2(g) $\rightarrow$ * + HNO_3(g) (R7) rather than via the NO_2 disproportionation (R8).

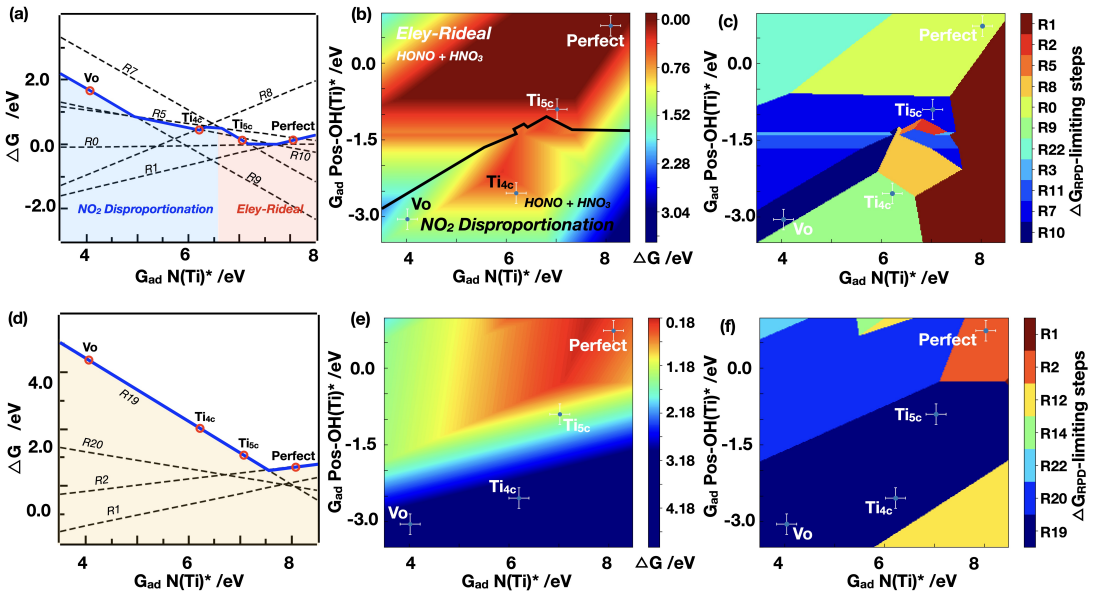

Fig. 5.4 (a) The reaction free energies of key elementary steps on all sites in the deNO$_2$ reactions under illumination conditions. Based on the scaling relationships between the adsorption free energies of adsorbates and descriptor (G_{ad} N(Ti)*), the reaction free energies (ΔG) can be described by the descriptor (G_{ad} N(Ti)*). The bold blue line denotes the 1D ΔG_{RPD}-limiting steps (determined by Eq. 3.9) for NO$_2$ + H$_2$O reactions on different sites. "NO$_2$ disproportionation" and "Eley-Rideal" denote that the reaction follows the NO$_2$ disproportionation and Eley-Rideal mechanisms, respectively. (b) The 2D (quasi) activity map with illumination is shown with two independent descriptors: adsorption free energies of N(Ti)* and Pos-OH(Ti)*. The Pos-OH(Ti)* denotes the adsorption free energy of OH(Ti)* in the positively charged system. The color bar denotes the limiting reaction free energies. (c) The 2D ΔG_{RPD}-limiting steps for the deNO$_2$ reactions on different sites under illumination condition. (d) The reaction free energies of key elementary steps for 2NO$_2$ + 2H$_2$O $\rightarrow$ H$_2$O$_2$ + 2HONO over all sites under illumination condition. (e) The 2D (quasi) activity map of H$_2$O$_2$ production with illumination is shown with two descriptors: adsorption free energies of N(Ti)* and Pos-OH(Ti)*, independently. The color bar denotes the limiting reaction free energies. (f) The ΔG_{RPD}-limiting steps for 2NO$_2$ + 2H$_2$O $\rightarrow$ H$_2$O$_2$ + 2HONO over all sites with illumination. The corresponding elementary steps are listed in **Table 5.1**.

5.3 H$_2$O$_2$ production during the photochemical reduction of NO$_2$ to HONO on anatase TiO$_2$(101) surface with illumination

I studied the H$_2$O$_2$ production separately. The 2D quasi activity map was established and is shown in **Fig. 5.4e**. Activity of the H$_2$O$_2$ production is lower than that of HNO$_3$ and HONO production on all sites. In other words, H$_2$O$_2$ must be a minor product, consistent with the previous experiments[97]. The ΔG_{RPD}-limiting step for the perfect surface is OH* dissociation(R2) and the ΔG_{RPD}-limiting step for the defective surface is (R19) H$_2$O(g) + O(Ti)* + * $\rightarrow$ H(O)* + OOH(Ti)* as shown **Fig. 5.4d, f**. For all studied sites, H$_2$O$_2$ formation follows:

$H_2O(g) \rightarrow H_2O(Ti)^* \rightarrow OH(Ti)^* \rightarrow O(Ti)^*$ [+ $H_2O(g)$] $\rightarrow H(O)^*$ + $OOH(Ti)^* \rightarrow H_2O_2(Ti)^*$

On the perfect surface, OH dissociation was facilitated by the photogenerated hole because of weakening of the bond of the adsorbed OH* group. However, the too strong binding energy of O* and OH* species on the defective surface inhibited the recombinative desorption and thus reduced the activity. Note that H_2O_2 was produced via the combination of H(O)* and OOH(Ti)*, instead of the previously proposed coupling of two OH* groups[97]. Because the two Ti sites are too far apart (3.75Å) and the OH* groups are strongly bonded.

In summary, it was found that the main products, HNO_3 and HONO, were identical over all sites and exhibited a high activity on the perfect surface and a lower one on the defective surface because of the strong binding of OH* species under both dark and illumination conditions. On the defective surface, the reduced Ti (i.e., the vacancy) captured the hole rather than the OH* group. Hence, the deNO$_2$ activities are not greatly improved on the defective surface with illumination. The main reaction pathways were not affected by the illumination. H_2O_2 is a minor product on the perfect surface with illumination, and it was formed via the combination of OOH(Ti)* and H(O)*.

5.4 Kinetic free energy profiles for deNO$_2$ under dark and illumination conditions

All the reaction mechanism discussions above are based on the global optimization of thermodynamics over diverse pathways. Calculated barriers are also surmountable, confirming the mechanisms above are feasible. **Fig. 5.5a** shows the reaction barriers in the production processes of HONO, HNO_3, and H_2O_2 on the perfect surface under dark and illumination conditions. Water dissociation, with a free energy barrier of 0.25 eV, and the following free energies associated with HONO and HNO_3 production are all downhill. In the case of H_2O_2 formation with illumination, OH* radical dissociation and combination of H* and OOH* groups are uphill with the low energy barriers of 0.09 eV and 0.05 eV, respectively. The free energies of the remaining associated steps are all downhill. The OH* dissociation and the final steps of HONO and HNO_3 formation are promoted by illumination. In addition, water dissociation is a stepwise process: electron transfer (ET) follows proton transfer (PT)[117]. Namely, OH^- captures the photogenerated hole after water deprotonation, yielding the OH radical. Hence, the HONO, HNO_3, and H_2O_2 production on the perfect surface is kinetically and thermodynamically favored. There are two possible reaction pathways for HONO and HNO_3 formation. **Fig. 5.4b** shows the optimal reaction mechanism and barriers of HONO, HNO_3, and H_2O_2 production on the defective surface, exemplified on Ti_{5c}, under dark and illumination conditions. The dissociated water in the Eley-Rideal pathway is con-

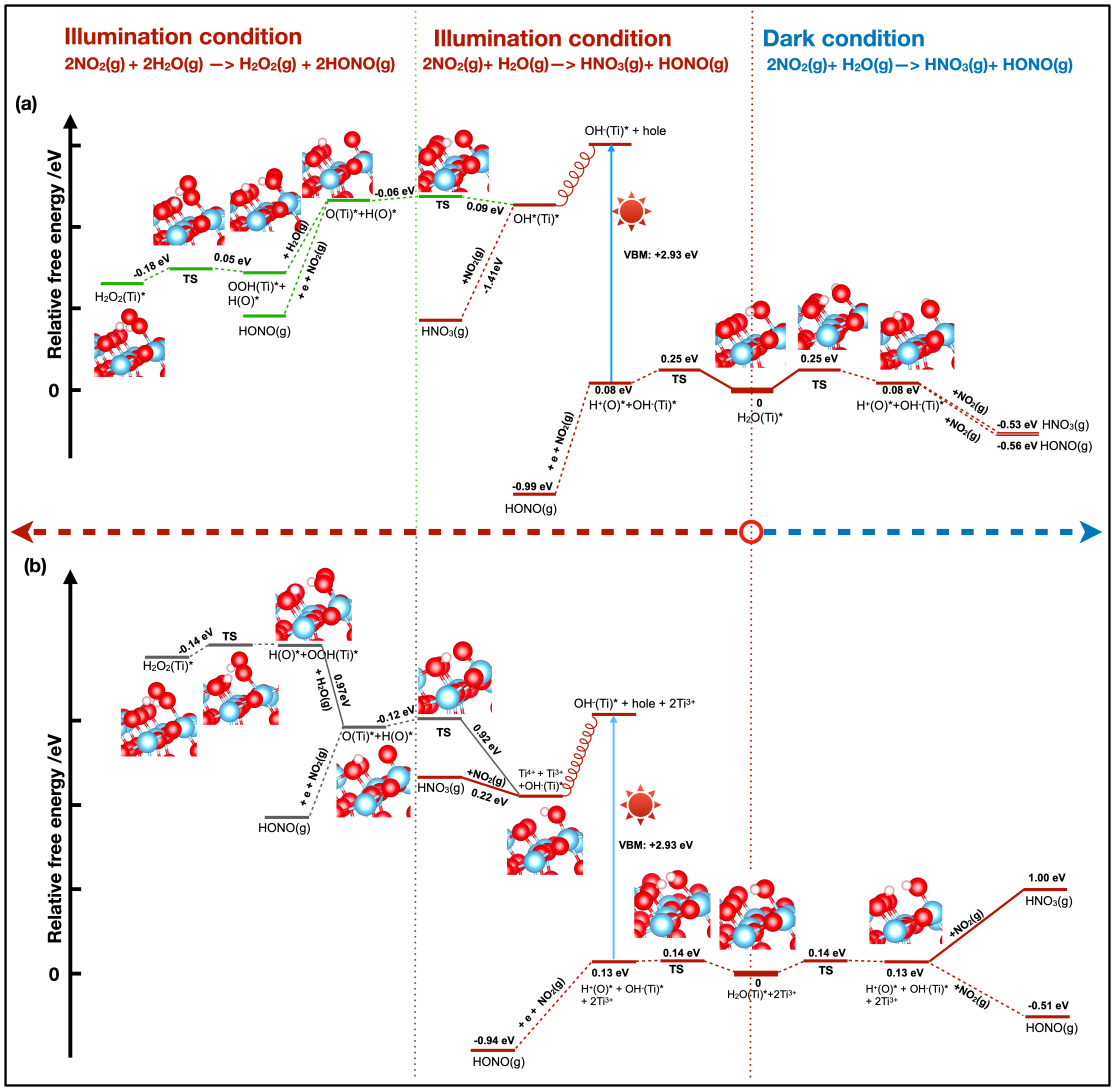

Fig. 5.5 Calculated reaction energies and barriers of each step for the deNO$_2$ reaction mechanisms on the (a) perfect and (b) defective (Ti_{5c}) surfaces under dark and illumination conditions, respectively. The solid lines denote the limiting steps. The VBM value was taken from experiment[8].

sumed by

(R6) H(O)* + NO$_2$(g) → HONO(g)

and

(R7) OH(Ti)* + NO$_2$(g) → HNO$_3$(g) + *

The second pathway includes the disproportionation of NO$_2$, and dissociated water is consumed by

(R9) NO(O)* + OH(Ti)* → HONO(g) + 2*

and

(R10)H(O)* + NO$_3$(Ti)* → HNO$_3$(g) + 2*

The energetic costs for OH(Ti)* + NO$_2$(g) → HNO$_3$(g) + * (R7) and 2NO$_2$ (g) + 2* → NO(O)* + NO$_3$(Ti)* (R8) are 0.87 eV and 1.01 eV under dark conditions, respec-

tively. In other words, disproportionation of NO_2 under dark conditions is a feasible pathway, which is consistent with the experiment[12]. However, HONO and HNO_3 production in the Eley-Rideal mechanism can be strongly facilitated by illumination, leading to the enhanced deNO$_2$ activity on Ti_{5c}, with a barrier of 0.22 eV. Assuming NO_2 disproportionation is not directly affected by illumination, the two paths are both feasible with illumination. As water dissociated, the hole was captured by the reduced Ti, instead of OH* and NO* groups. H_2O_2 production with illumination proceeds along the following pathway:

$H_2O(g) \rightarrow H_2O(Ti)^* \rightarrow OH(Ti)^* \rightarrow O(Ti)^*$ [+ $H_2O(g)$] $\rightarrow H(O)^*$ + $OOH(Ti)^* \rightarrow H_2O_2(Ti)^*$

The dissociative barrier of OH* groups was calculated to be 0.92 eV, which is consistent with the report published earlier[118]. The thermodynamic free energies for the $O(Ti)^*$ + $H_2O(g)$ reaction has reached 0.97 eV. These can be ascribed to the too strong interactions of the O* species with the defective surface, which can be explained by the fact that the excess electron is transferred to the adsorbates from the reduced Ti site. Thus, it is difficult to produce H_2O_2, although the combination of $OOH(Ti)^*$ and $H(Ti)^*$ to H_2O_2 is a barrierless process. In short, the calculated kinetic results are consistent with the prediction from energetic global optimization of reaction phase diagram analysis.

5.5 Summary

In this work, I have employed an improved scheme to study the mechanisms of photoassisted deNO$_2$ reactions on the active sites of the anatase TiO_2(101) surface. The electronic structures and energies were calculated by using a GGA + LZ functional, which significantly improved the accuracy (comparable to calculations with the hybrid HSE06 functional) while maintaining the efficiency of normal GGA calculations. In addition, a novel algorithm was applied to study all possible reaction pathways and to obtain a global optimization of the limiting energies. It was found that the activity on the perfect surface is higher than on a defective one, because the strong OH* adsorption inhibits its combination with NO_2. It was found the photogenerated hole is more important for the perfect surface in tuning the reactivity. Because the hole is trapped by a reduced Ti on the defective surface, it has no effect on the adsorption energy of OH* species on the oxygen vacancy. In contrast, the OH* adsorption energy on a perfect surface can be weakened in the presence of the photogenerated hole, resulting in enhanced OH* conversion. This work proved the concept that the tunable reactivity in a charge-assisted process and diverse reaction pathways in photocatalysis are two methods that break the conventional scaling relation and the activity volcano plot limit under dark conditions, which is a quite critical insight for the design of catalyst.

6 | Activity and reaction mechanism mapping of photocatalytic deNO processes on titania surfaces

As discussed in last chapter, the photogenerated hole can promote the oxidative reactions and oxidize the NO_x into higher oxidization state with active oxygen or OH radicals[2, 7]. However, the accompanying pollution, i.e. nitrate and nitrite, is troublesome. NO_x can also be reduced with illumination[2, 4, 97]. The photogenerated electrons promote the reductive reactions and convert NO_x into harmless N_2, which can avoid secondary pollution problems[4]. Therefore, many studies have focused on the photoreduction of NO_x on TiO_2 surfaces, especially the decomposition of NO into N_2 and O_2, which was considered as a desirable photocatalytic denitrification process[2]. It was reported that NO can be reduced to N_2O and N_2 over TiO_2 powders, but N_2O is the major product[119]. Many efforts have been made to increase the selectivity of N_2 in photocatalytic deNO over TiO_2[119, 120, 121, 122]. A notable finding by Wu and Krol is that oxygen vacancies are the active centers for denitrification. Increasing the number of oxygen vacancies, such as by doping the TiO_2 with iron, can improve the N_2 selectivity[4]. Note that oxygen vacancies are not typically present on the anatase surfaces, but they can be created by experimental techniques[4, 123]. Additionally, the reaction mechanism of photo-decomposition of NO is dispute. Wu and Krol proposed that two NO molecule can be directly dissociated to two surface oxygen and two nitrogen atoms, which can be easily coupled into N_2 and O_2[4]. On the reduced rutile TiO_2 (110) surface, however, Xu and Cao suggested that the trans-$(NO)_2$ dimers can be formed at Vo and adjacent $Ti_{\mathbf{5c}}$ sites, which can then be converted to N_2O[123]. In addition to the oxygen vacancies, it is well-known crystalline structures (anatase and rutile) can be quite different in reactivity. However, no significant differences between anatase and rutile were observed in experiments. The comparison of N_2 selectivity in mechanism between (anatase and rutile) titania surfaces can also provide useful guidance for catalyst design in the future.

In this work, I employed a graph theory based algorithm to study possible re-

(R0) NO(g) + * → NO(Ti)*
(R1) NO(Ti)* + NO(g) → N_2O_2(Ti)*
(R2) * + 2NO(g) → N_2O_2(Ti)*
(R3) N_2O_2(Ti)* + * → N_2O(Ti)* + O(Ti)*
(R4) 2* + NO(g) → O(Ti)* + N(O)*
(R5) 2* + NO(g) → O(Ti)* + N(Ti)*
(R6) N(O)* → N(Ti)*
(R7) N(O)* + N(Ti)* → 2* + N_2(g)
(R8) N(Ti)* + NO(g) → N_2O(Ti)*
(R9) N_2O(Ti)* → O(Ti)* + N_2(g)
(R10) N_2O(Ti)* → N_2(g) + O(O)*
(R11) N(O)* + NO(g) → N_2O(O)*
(R12) N_2O(O)* → N_2(g) + O(O)*
(R13) N_2O(O)* → N_2O(Ti)*
(R14) O(O)* → O(Ti)*
(R15) 2N(Ti)* → 2* + N_2(g)
(R16) 2O(O)* → 2* + O_2(g)
(R17) 2N(O)* → 2* + N_2(g)
(R18) 2O(Ti)* → * + O_2(Ti)*
(R19) O(O)* + O(Ti)* → * + O_2(Ti)*
(R20) O_2(Ti)* → * + O_2(g)
(R21) N_2O(Ti)* → * + N_2O(g)
(R22) N_2O(O)* → * + N_2O(g)
(R23) 2hole + O_2(Ti)* → Pos-O_2(Ti)*
(R24) Pos-O_2(Ti)* → * + O_2(g)

Table 6.1 All considered elementary steps for 2NO(g) → N_2(g) + O_2(g) and 4NO(g) → N_2O(g) + O_2(g) reactions.

action pathways[5] and obtain the collection of reaction pathways prior to energetic comparison. Then, I calculated the adsorption energies of relevant intermediates in deNO on a set of active sites over perfect and defective anatase TiO_2(101) surfaces and rutile TiO_2(110) surfaces in both dark and illumination conditions, using our recently developed density functional with appropriate band gap and localization error corrections[46], and charge correction scheme[48]. At last, the reaction phase diagrams were established based on the global (thermodynamic) energy optimization. Herein, my aim is to elucidate the deNO activity and selectivity of different active sites on the TiO_2 surfaces under dark and illumination conditions.

According to the experimental observations, I considered two main reactions: 2NO(g) → N_2(g) + O_2(g) and 4NO(g) → N_2O(g) + O_2(g). 25 possible elementary steps were considered as listed in **Table 6.1** and 3109 possible reaction pathways were obtained with the CatRPD code[124] to build the reaction networks. In short, all possible reaction pathways were obtained by the free combination of all forward and backward elementary steps. At a given active site, I first determine the most difficult steps in

the internal comparison among elementary steps. Then, the optimal reaction pathway should be the one with minimal free energy change (ΔG) in external comparison among all possible pathways with Eq. 3.9.

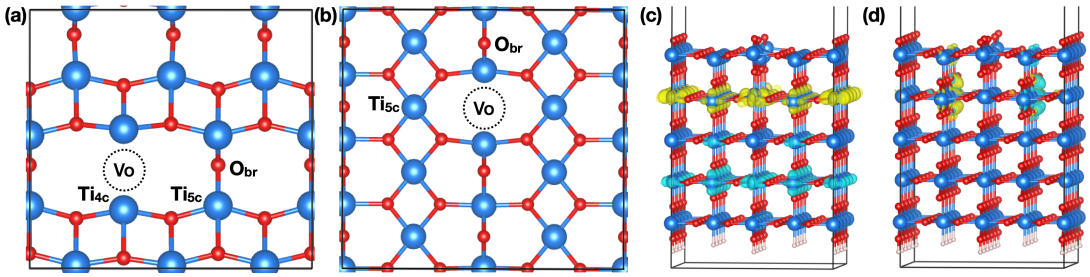

Fig. 6.1 Top view and nomenclature of the sites on the defective anatase TiO_2(101) surface (a) and rutile TiO_2(110) surface (b): Vo denotes the oxygen vacancy; Ti_{4c} denotes the 4-fold coordinated Ti; Ti_{5c} denotes the 5-fold coordinated surface Ti site; O_{br} denotes the bridging oxygen on the surface. Spin distributions in the singlet state of a neutral oxygen vacancy on the rutile TiO_2(110) surface, as obtained from PBE without (c) and with (d) the Lany-Zunger correction. The two spin directions are distinguished by color. Cyan, red, and pink denote Ti, O, and H, respectively.

I calculated the adsorption free energies of N, O, N_2O_2, N_2O, O_2 on seven different active sites: oxygen vacancy site on anatase TiO_2(101) surface (A-Vo) and rutile TiO_2(110) surface (R-Vo), four-fold coordinated Ti site on the defective anatase TiO_2(101) surface (D-A-Ti_{4c}), five-fold coordinated Ti site on the defective anatase TiO_2(101) surface (D-A-Ti_{5c}) and rutile TiO_2(110) surface (D-R-Ti_{5c}), five-fold coordinated Ti site (Ti_{5c}) on the perfect anatase TiO_2(101) surface (P-A-Ti_{5c}) and rutile TiO_2(110) surface (P-R-Ti_{5c}), respectively.(see in **Fig. 6.1a, b**) Note that I have also considered the Ti_{5c}(Vo) site in my calculations but the adsorbates tend to move to the Vo site from Ti_{5c}(Vo) site after the relaxation. The nomenclature is the same here for all intermediates, unless stated otherwise. As shown in **Fig. 6.1c, d**, PBE calculations show that the electrons of neutral oxygen vacancy delocalize in the whole slab while the PBE + LZ calculations show that two electrons of neutral oxygen vacancy localize on two subsurface Ti atoms, respectively. Neutral oxygen vacancy of rutile (110) surface is a biradical singlet state. These results are consistent with higher level (HSE06) calculations in the published paper[125, 76].

The adsorption free energies of N was chosen as the descriptor to establish the correlation relationships with the adsorption energies of other considered adsorbates. As shown in **Fig. 6.2**, the scaling relations show good linearity. Thus, the adsorption free energy of each considered species and the free energy of each elementary step can be well described by the descriptor.

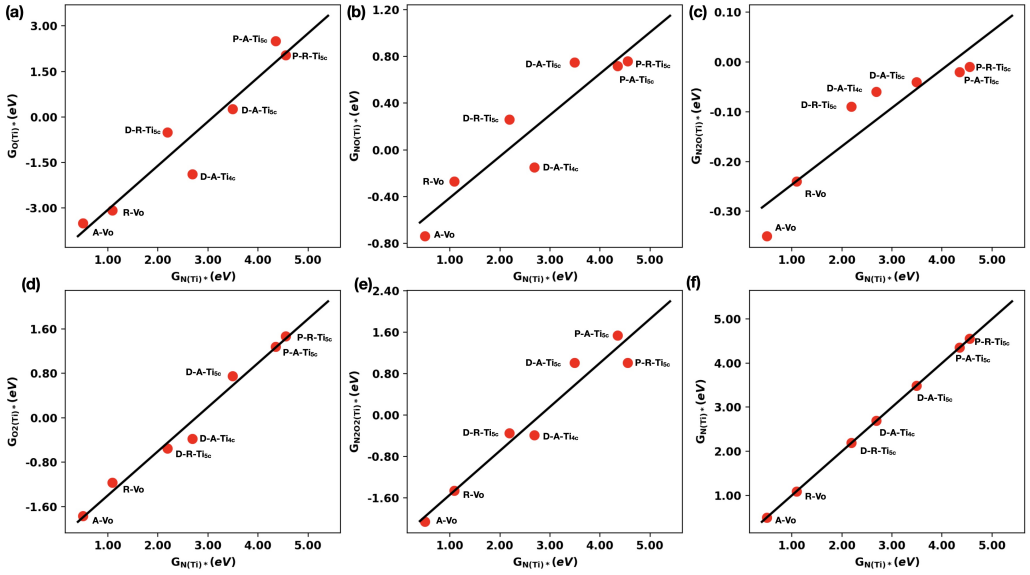

Fig. 6.2 Scaling relations of the adsorption energies for (a) O*, (b) NO*, (c) N_2O*, (d) O_2*, (e) N_2O_2*, (f) N* on the different active sites of anatase $TiO_2(101)$ and rutile $TiO_2(110)$ surfaces. The adsorption free energies of N(Ti)* was chosen as the descriptor. All the free adsorption energies were calculated with reference to the energy of the gas molecules NO, O_2. A-Vo and R-Vo denote the oxygen vacancies on the surfaces of anatase $TiO_2(101)$ and rutile $TiO_2(110)$, respectively. D-A-$Ti_{\mathbf{5c}}$ and D-R-$Ti_{\mathbf{5c}}$ denote the five-fold coordinated Ti sites on the defective surfaces of anatase $TiO_2(101)$ and rutile $TiO_2(110)$, respectively. D-A-$Ti_{\mathbf{4c}}$ denotes the four-fold coordinated Ti site on the defective anatase $TiO_2(101)$ surface. P-A-$Ti_{\mathbf{5c}}$ and P-R-$Ti_{\mathbf{5c}}$ denote the five-fold coordinated Ti sites on the perfect anatase $TiO_2(101)$ and rutile $TiO_2(110)$ surfaces, respectively.

6.1 Activity and mechanism mapping of NO decomposition without illumination

As O* and O_2* are two key species for O_2 production, $G_{\mathbf{ad}}$ O(Ti)* was chosen as the second descriptor for establishing two dimensional maps. The (quasi) activity and selectivity maps of deNO reactions over diverse TiO_2 surfaces/sites are shown in **Fig. 6.3**. Under dark condition, it enables to produce N_2 on defective TiO_2 surfaces, while it is selective for N_2O production on intact TiO_2 surfaces as shown in **Fig. 6.3a, b**. D-A-$Ti_{\mathbf{4c}}$ exhibits the highest activity to produce N_2 and the main $\Delta G_{\mathbf{RPD}}$-limiting steps are likely to be N_2O_2 formation, O_2 formation and O_2 desorption as shown in **Fig. 6.3c**, because of similar $\Delta G_{\mathbf{RPD}}$ for these steps (around 0.01 eV). However, oxygen vacancies are inactive because a high reaction energy of around 1.20 eV. Two perfect rutile and anatase surfaces have also low activity ($\sim$ 1.0 eV uphill in reaction free energies) and the main $\Delta G_{\mathbf{RPD}}$-limiting steps are NO adsorption and N_2O_2 dissociation as shown in **Fig. 6.3c**. Diverse reaction pathways are compared to produce N_2 and N_2O over titania surfaces. D-A-$Ti_{\mathbf{4c}}$ and D-R-$Ti_{\mathbf{5c}}$ follow the same reaction pathway that N_2

is produced via N_2O* dissociation: $2NO(g) \rightarrow N_2O_2(Ti)^* \rightarrow N_2O(Ti)^* \rightarrow N_2(g) + O(Ti)^*$ (path1). N_2 production on oxygen vacancies follow the similar reaction pathway: $2NO(g) \rightarrow N_2O_2(Ti)^* \rightarrow N_2O(Ti)^* \rightarrow N_2(g) + O(O)^*$(path2). As D-A-$Ti_{5c}$ is located at the boundary of path1 and path3, N_2 can be produced via path1 or path3: $NO(g) \rightarrow NO(Ti)^* \xrightarrow{+NO(g)} N_2O_2(Ti)^* \rightarrow N_2O(Ti)^* \rightarrow N_2(g)$. At Ti_{5c} sites on perfect surfaces, N_2O is formed via path4: $NO(g) \rightarrow NO(Ti)^* \xrightarrow{NO(g)} N_2O_2(Ti)^* \rightarrow N_2O(Ti)^* \rightarrow N_2O(g)$, which is consistent with the calculations by Xu et al[123]. Note that the extra electrons can migrate to adsorbates from defective surfaces[40, 57, 126, 127], especially at the oxygen vacancies. Therefore, the oxygen vacancies exhibit strong reactivity, but low catalytic activity for deNO reactions.

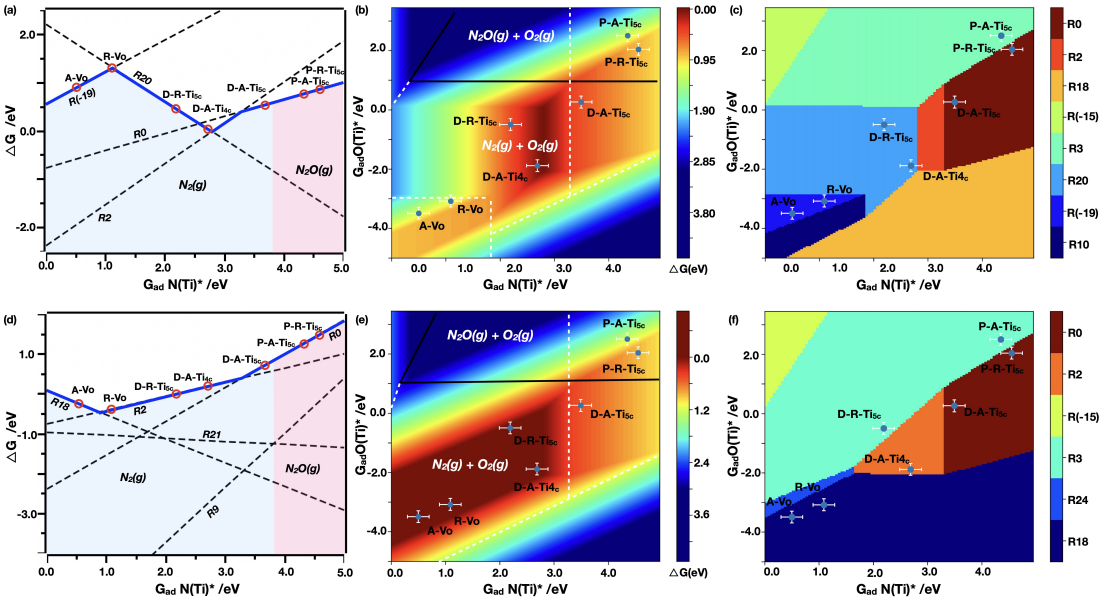

Fig. 6.3 (a) The reaction free energy change of key elementary steps on all sites without illumination. The bold blue line denotes the 1D ΔG_{RPD}-limiting steps for NO decomposition reactions on different sites, which are determined with Eq. 3.9. (b) The 2D quasi activity and selectivity map is shown with respect to the two descriptors (adsorption free energies of N(Ti)* and O(Ti)*) independently without illumination. The color bar denotes the ΔG_{RPD}-limiting energies. (c) The ΔG_{RPD}-limiting steps for the deNO over all considered sites without illumination. (d) The 1D reaction free energy change of key elementary steps on each site with illumination. (e) The 2D quasi activity and selectivity map is shown with respect to the two descriptors (adsorption free energies of N(Ti)* and O(Ti)*) independently with illumination. The color bar denotes the ΔG_{RPD}-limiting energies. (f) The ΔG_{RPD}-limiting steps for the deNO on all sites with illumination. A-Vo and R-Vo denote the oxygen vacancies on the anatase TiO_2(101) surface and rutile TiO_2(110), respectively. D-A-Ti_{5c} and D-R-Ti_{5c} denote the five-fold coordinated Ti sites on the defective anatase TiO_2(101) and rutile TiO_2(110) surfaces, respectively. D-A-Ti_{4c} denotes the four-fold coordinated Ti site on the defective anatase TiO_2(101) surface. P-A-Ti_{5c} and P-R-Ti_{5c} denote the five-fold coordinated Ti sites on the perfect anatase TiO_2(101) and rutile TiO_2(110) surfaces, respectively. The corresponding elementary steps are listed in **Table 6.1**

6.2 Activity and mechanism mapping of NO decomposition with illumination

In principle, there are two main possibilities to improve the activity with illumination. One is to improve the reaction free energies of limiting steps in dark condition by photogenerated carriers. The other one is to construct new reaction pathways with higher activity. As the reaction pathways were all already determined before energetic comparison, it has been a global optimum in energies in dark condition. In other words, a photo-generated carrier can affect the adsorption energies of key intermediates and break the strong correlation shown in **Fig. 6.2**. Hence, I reanalyzed the (quasi) activity and selectivity map, as well as the adsorption energies of limiting steps under illumination condition. Herein, I mainly address the activity variation of oxygen vacancies with illumination. Because the generated O_2* species on oxygen vacancies have strong interactions with surfaces and are difficult to desorb from surface. Thus, I studied the effect of two photo-generated holes on the O_2 desorption. It was found that dioxygen can be produced by the coupling of two O(Ti)* species over most sites with illumination. It was found that the holes were trapped by the adsorbed O_2 species and oxidized O_2^{2-} into O_2^- at oxygen vacancies, weakening the adsorption of O_2 species.

As shown in **Fig. 6.3d, e**, the N_2 selectivity is not influenced by illumination, but the activities are significantly improved by illumination on oxygen vacancies, which is consistent with experimental reports[7, 121]. It exhibits the highest activity on oxygen vacancies and the optimal reaction pathways remain unchanged on all studied sites except oxygen vacancies. On oxygen vacancies, the optimal reaction pathway changes to path1 and the main $\Delta G_{\mathbf{RPD}}$-limiting step is O_2 formation, which is realized via the coupling of two O* species **Fig. 6.3f**. It should be mentioned that our method finally provides the most preferred reaction pathways based on thermodynamic analysis. It was found that path3 can produce N_2 at oxygen vacancies using the same $\Delta G_{\mathbf{RPD}}$-limiting step as path1. Thus, N_2 can be produced at oxygen vacancies through both path1 and path3. Importantly, as shown in **Fig. 6.3d**, it was found that N_2O desorption (R21) is comparable with N_2O dissociation (R9). Thus, it is possible to produce N_2O on defective surfaces with the same $\Delta G_{\mathbf{RPD}}$-limiting steps as N_2 production. In other words, both N_2 and N_2O can be produced with similar activity on defective surfaces. In addition, it was found that N_2 and N_2O are produced via the dissociation of N_2O_2*, instead of the direct NO dissociation. As the NO dissociative energy is too high, $\sim$1.16 eV, on A-Vo site (NO(Vo)* + * $\rightarrow$ N(Vo)* + O(Ti)*).

6.3 Summary

In a short summary, it is thermodynamically feasible to produce N_2 on defective TiO_2 surfaces, whereas it is more selective to produce N_2O on perfect TiO_2 surfaces. The (quasi) activity was significantly enhanced by photo-generated holes and the photocatalytic decomposition of NO into N_2 is thermodynamically feasible on defective titania surfaces. The low efficiency observed in experiments could be attributed to the weak adsorption of N_2O, which make it easy to desorb from surfaces rather than N_2O* dissociation to N_2. Notably, N_2 production is favored by N_2O dissociation, rather than the paths of direct NO dissociation. This is an important finding that N_2 production has to via N_2O* path. The thermodynamic analysis based on reaction phase diagram and global energy optimization provides a fundamental limit of enhancing N_2 selectivity. In the following, I performed kinetic studies for photocatalytic NO decomposition over titania surfaces.

7 | A fundamental limit of selectivity in photocatalytic denitrification over titania surfaces

7.1 Microkinetic modeling of photocatalytic deNO over titania surfaces

Based on the above discussions, I mainly focused on the kinetics of photocatalytic deNO on Vo site of anatase $TiO_2(101)$ surface, because oxygen vacancy was usually found with relatively high thermodynamic feasibility for N_2 selectivity. A systematic microkinetic model was conducted based on DFT calculations (as shown in **Fig. 7.1**) and experimental conditions to study the rate-limiting steps and selectivity of products. The detailed input parameters for microkinetic modelling are listed in **Table 7.1**.

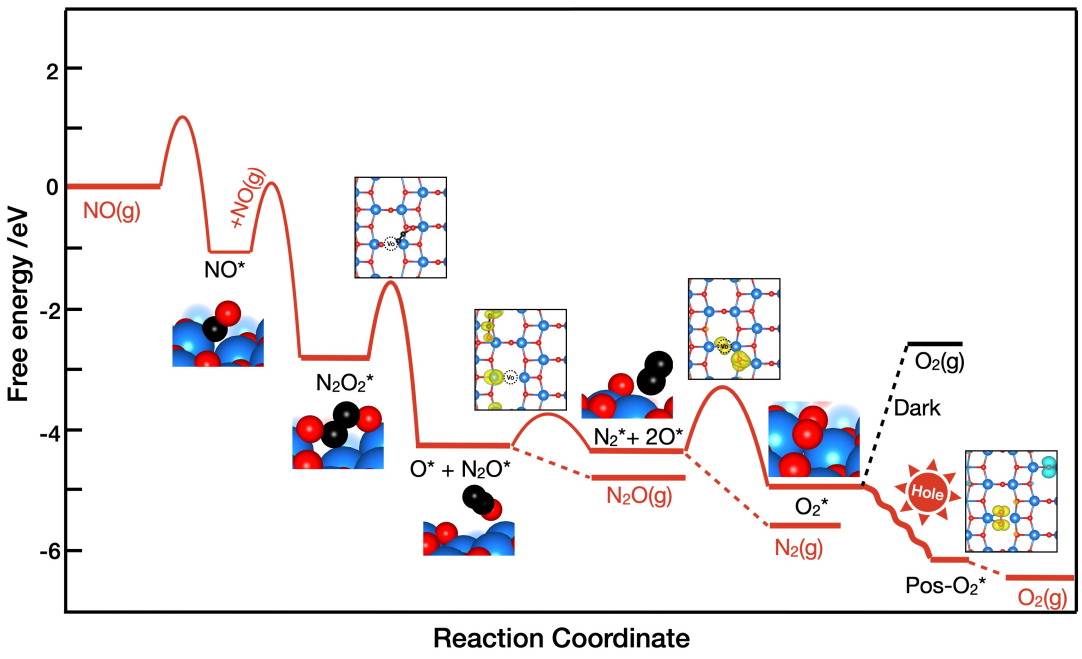

Fig. 7.1 Free energy profile for photocatalytic decomposition of NO on the oxygen vacancy of anatase $TiO_2(101)$ surface. The spin densities of the key transition states are illustrated. Blue, red and black denote Ti, O and N atoms, respectively. Pos-O_2* denotes the O_2 adsorption in positively charged system.

elementary steps	Zeolite(298K)		A-Vo(493K)	
	Ea / eV	ΔH /eV	Ea / eV	ΔH /eV
NO(g) + * → NO*		-2.63		-2.24
NO* + NO(g)→ N_2O_2*		-1.45		-2.91
2NO(g) + 2* → N_2O_2*		-4.08		-5.15
N_2O_2* + * → N_2O* + O*	0.09	-1.37		
N_2O* + * → N_2* + O*	0.04	-2.50		
2O* →O_2*	0.30	0.17		
N_2O_2* + # → N_2O# + O*			1.25	-1.44
N_2O# + # → N_2# + O#			0.58	-0.09
O* + O# → O_2* + #			1.04	-0.59
O_2* → O_2(g) + *		2.76		2.68
O_2* + 2hole → Pos-O_2*	-	-	-	-
Pos-O_2* → O_2(g) + *		0.87		0.83
N_2* → N_2(g) + *		0.84		
N_2# → N_2(g) + #				0.43
N_2O* → N_2O(g) + *		1.28		
N_2O# → N_2O(g) + #				0.68

Table 7.1 Thermodynamic and kinetic data of deNO reactions on the Ti site of the modified zeolite and Vo site on the anatase TiO_2(101) surface. # and * denote the different active sites.

As shown in **Fig. 7.1**, a trans-N_2O_2* could be formed via the coupling of two gas phase NO molecules with energy barrier of 2.31 eV (path1) or via Eley-Rideal (E-R) mechanism with two lower energy barriers(1.15 eV) (path3). Then, N_2 is formed in such a way: N_2O_2(Ti)* → N_2O(Ti)* → N_2(g). O_2* is formed via the coupling of two O* species and the formed O_2* has strong interaction with the catalyst. Under illumination condition, the photo-generated holes weaken the O_2* adsorption and the photo-generated electrons are supposed to reduce the oxygen vacancy. The optimal reaction path was indicated by the red lines in **Fig. 7.1**. The free energy barriers associated with N_2 production are uphill. It is found that the main rate determining steps are N_2O_2* formation, N_2O_2* dissociation and O_2 * formation with energy barriers of 1.15 eV, 1.25 eV and 1.04 eV, respectively. Notably, N_2O is favored to desorb in comparison with N_2O dissociation. Therefore, the competing N_2O production and the high kinetic barriers of rate limiting steps lead to the inefficient N_2 production at A-Vo site. This is generally consistent with the experimental results that the major product is N_2O[119]. I have analyzed the electronic structures in photocatalytic processes and the spin densities of key transition states are shown in **Fig. 7.1**. The adsorbed N_2O_2* has a binding with Vo and $Ti_{\mathbf{5c}}$ and captures the electrons from oxygen vacancy, weakening the N-O bond. In transition state of N_2O dissociation, an electron transfers to N_2O from oxygen vacancy, causing bending of liner N_2O and shortening the Ti-O and Ti-N bonds from 2.80 Å to 2.35 Å, facilitating N-O bond breaking. The two extra electrons in oxygen

vacancy are trapped by two O species in the transition state of O_2 formation. Finally, the formed O_2^{2-} is oxide to O_2^- by the photogenearted hole. Therefore, the oxygen vacancy facilitates the bond breaking and increases the reactivity under illumination condition.

7.2 Microkinetic modeling of photocatalytic deNO on Ti modified Y-zeolite

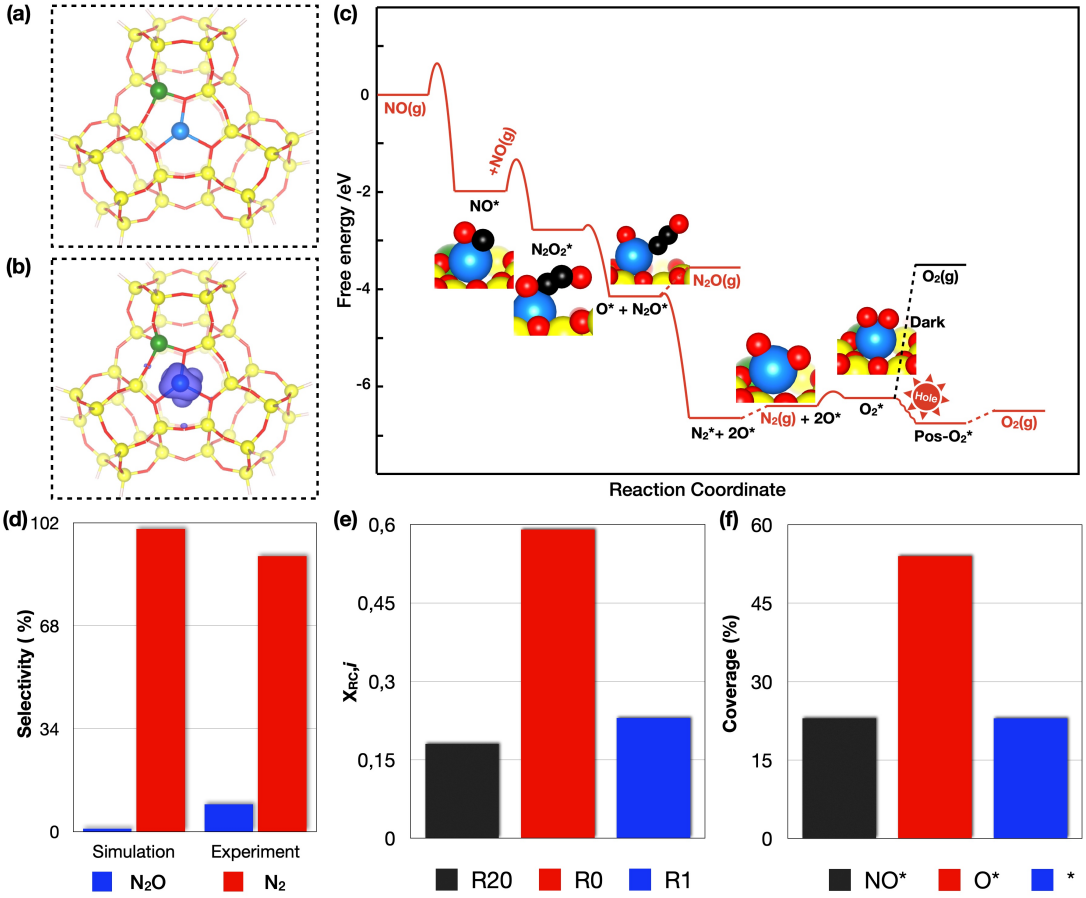

Fig. 7.2 (a) Ti modified Y-zeolite cluster model. (b) Spin density distributions in the Ti-modified Y-zeolite cluster with isovalue of 0.005 a_0^{-3} (a_0: Bohr radius). (c) Energy profile for photo-decomposition of NO on Ti site of modified zeolite. (d) The simulated and experimental selectivities in photocatalytic decomposition of NO on Ti-modified zeolite. (e) The degree of rate control (DRC) analysis in the phtocatalytic deNO processes for N_2 production on zeolite. (f) The coverage of species distribution at steady state. Pos-O_2* denotes the O_2 adsorption in positively charged system. * denotes the active site Ti of zeolite. Cyan, red, yellow, green and pink denote Ti, O, Si, Al and H atoms, respectively. The corresponding elementary steps are listed **Table 6.1**.

It was observed that the maximum conversion of NO is only 1% on the reduced TiO_2 and 4.5% on the Fe-doped TiO_2, respectively[4]. The observed activity and selectivity is still low, so it is crucial to find the chemical origins of the low efficiency of NO photo-decomposition. In contrast, there is an exceptional success found in Ti-modified zeolite,

where the N_2 selectivity is much improved (>90%)[121]. It can be quite helpful in the choice of experiments as far as the fundamental limit of photocatalytic denitrification on titania surfaces was understood.

elementary step(i)	r_i	Z_i	$X_{\mathbf{RC,i}}$
NO(g) + * → NO*	1.38e-05	3.39e-28	0.59
NO* + NO(g)→ N_2O_2*	1.38e-05	4.42e-23	0.23
N_2O_2* + * → N_2O* + O*	1.38e-05	2.33e-24	0.00
N_2O* + * → N_2* + O*	1.38e-05	3.58e-29	0.00
2O* →O_2*	1.38e-05	1.00e-01	0.00
O_2* + 2hole → Pos-O_2*	-	-	-
Pos-O_2* → O_2(g) + *	1.38e-05	3.47e-01	0.18
N_2* → N_2(g) + *	1.38e-05	7.30e-01	0.00

Table 7.2 Kinetic Data, r_i, the reversibility (Z_i), and $X_{\mathbf{RC,i}}$, for each elementary reaction step in the deNO over Ti modified zeolite. * denotes the Ti site of zeolite. Note that the rate r_i is equal to the difference between the forward (r_i^+) and reverse (r_i^-) rates, namely, $r_i = r_i^+ - r_i^-$

The unique performance of Ti-modified zeolite frameworks, where the photocatalysts were prepared by ion exchange techniques[121], was ascribed to the observed highly dispersed molecular-sized titanium oxide species incorporated within zeolite frameworks, which was not observed in TiO_2 powder by ESR and XAFS measurements [120, 121]. To figure out the distinctive behaviors on Ti-modified zeolites, I built a Y-zeolite model, where a Si atom is replaced by a Al atom and a Ti atom is introduced in the center of six-ring. Al atom takes one electron from Ti atom and oxides Ti^0 into Ti^+. The side view and spin density of Ti modified Y-zeolite are shown in **Fig. 7.2a, b**. A microkinetic model at steady state was performed to study the key factors of N_2 selectivity, compared to N_2O production. A comparative analysis was made to understand the exceptional success of improved N_2 selectivity in Ti-modified zeolite with respect to titania surfaces. It was found the adsorption energies of N_2O must be strengthened to enhance the N_2 selectivity. The details for microkinetic modelling are listed in **Table 7.1**. The calculated free energy diagram is shown in **Fig. 7.2c**. The reaction pathway is consistent with that of the A-Vo. The free energies associated with N_2 production are barrierless except the N_2O_2* formation. N_2O_2* prefers to form via E-R mechanism with two lower energy barriers of 0.65 eV. Note that N_2O* adsorption is stronger than that on titania surfaces and N_2O desorption is uphill on Ti-modified Y-zeolite. The intrinsic activity and selectivity of N_2 and N_2O, and the coverage of intermediates at steady state are summarized in **Fig. 7.2d, e**. The simulated N_2 selectivity on the Ti-modified zeolite is up to 100%, as shown in **Fig. 7.2d**, which is basically consistent with the experimental report of 91%[121]. The DRC (degree of rate control) $X_{\mathbf{RC,i}}$ (see the definition in

ref.[93]) was usually used to analyze the importance of each elementary step i in the studied mechanism[20, 92, 93]. The larger $X_{RC,i}$ value of a given elementary step i, the greater effect it has on the whole reaction rate. Namely, the elementary step with largest $X_{RC,i}$ in the proposed mechanism is the rate determining step. The DRC of elementary steps R0 (NO adsorption), R1 (the association of NO(Ti)* and NO(g)) and R20 (O_2 desorption) are 0.59, 0.23, 0.18 in the proposed phothocatalytic deNO reaction mechanisms, respectively (**Fig. 7.2e and Table 7.2**). The DRC are negligibly small for all the other elementary steps. Thus, the R0 (NO adsorption) is the main kinetically rate limiting step in photocatalytic deNO processes on Ti-modified Y-zeolite. As shown in **Fig. 7.2f**, the coverage of O*, free active site, and NO* are 54%, 23%, 23%, respectively. This implies O* species have a relatively strong adsorption and they are hard to be coupled to dioxygen. The desorption of NO* species is suppressed and there are also some available free active sites. Therefore, the N_2 selectivity and yield can be further increased by weakening O* adsorption and increasing N_2O* adsorption and dissociation. This should be a new strategy for photocatalyst design in the future.

7.3 Summary

Microkinetic modeling was applied to understand the kinetic factors at experimental conditions, clarifying the fundamental limits in deNO on titania surfaces. Although it was found that the deNO activity can be significantly enhanced under illumination condition by weakening the O_2 adsorption, the limiting factor is that the N_2O and N_2 productions share the same N_2O* species. A exceptional character of Ti-modified zeolites with good N_2 selectivity can be attributed to very strong N_2O* adsorption, compared to the weak N_2O adsorption and low N_2 selectivity over titania surfaces. Therefore, N_2O* is a key intermediate to enhance N_2 selectivity and deNO activity. I demonstrate here the reaction phase diagram analysis can be a good tool to obtain a global picture of activity (and selectivity) trend over different reaction sites. Combined with microkinetic modelling, the key factors of catalytic failure and exceptional success can be rationalized well with relatively low computational cost, which can be a good choice for catalyst design.

8 | Conclusion

In this work, I have adopted an improved scheme to study the mechanisms of photo assisted deNO$_x$ reactions on the active sites of the various titania surfaces, perfect and defective anatase TiO_2(101) and rutile TiO_2(110) surfaces. On the one hand, the electronic structures and energies were calculated using the GGA + LZ functional, which greatly improved the accuracy (comparable to the calculations using the hybrid HSE06 functional) while maintaining the efficiency of normal GGA calculations. On the other hand, a novel algorithm was applied to study all possible reaction pathways and to obtain a global optimization of the limiting energies. Additionally, microkinetic modeling was applied to understand the kinetic factors under experimental conditions, clarifying the fundamental limits in deNO over titania surfaces.

1. I investigated the reaction mechanisms of NO_2 and H_2O on anatase TiO_2(101) surface. It was found that the major products are HONO and HNO_3 and the minor product is H_2O_2. The activity is higher on the perfect surface than on a defective surface. Because the strong OH* adsorption inhibits its association with NO_2 on the defective surface. The photogenerated carriers favor the tuning of the reactivity of perfect surface while having no effect on the reactivity of defective surface. Because the OH* adsorption energy on the perfect surface can be weakened in the presence of the photogenerated hole, resulting in enhanced OH* conversion. In contrast, the hole is trapped by a reduced Ti on the defective surface and thus the adsorption energy of OH* species on the oxygen vacancy remains unchanged. (Published in JPCL)

2. I have systematically investigated the thermodynamics of photocatalytic decomposition of NO (deNO) into N_2O, N_2 and O_2 on a variety of active sites of anatase and rutile TiO_2 surfaces. The photogenerated carries can significantly improve the activity. It was found that it is selective to N_2 production on defective TiO_2 surfaces, whereas it is more selective to N_2O production on perfect TiO_2 surfaces. N_2 production shared the same N_2O* species with N_2O production and N_2 was not produced via NO direct dissociation. (Under review in JPCL)

3. Ti-modified zeolite performed distinctive N_2 selectivity in comparison to titania

surfaces. Microkinetic simulations of Ti-modified zeolite and TiO_2 revealed that the strong adsorption of N_2O* led to the good selectivity for N_2 production. Consequently, the strong adsorption of N_2O plays an important role in improving N_2 selectivity and denitrification activity. (Under review in JPCL)

It was indicated that the reaction phase diagram analysis can be a useful tool to obtain a global picture of activity (and selectivity) trend over various active sites, while the tunable reactivity in a charge-assisted process can be achieved by breaking the conventional scaling relationships and the limits of activity volcano plot under dark conditions. In combination with microkinetic modelling, the key factors for catalytic failure and exceptional success can be well rationalized at relatively low computational cost, which can be an important option for catalyst design.

LIST OF PUBLICATIONS

1. Guo, P.; Fu, X.; Deák, P.; Frauenheim, T.; Xiao, J. Activity and Mechanism Mapping of Photocatalytic NO_2 Conversion on the Anatase TiO_2(101) Surface. J. Phys. Chem. Lett. 2021, 12 (32), 7708–7716.

2. Guo, P.; Deák, P.; Fu, X.;Frauenheim, T.; Xiao, J. A fundamental limit of selectivity in photocatalytic denitrification over titania, J. Phys. Chem. Lett. 2022, 13, 11051–11058.

REFERENCES

[1] Thirupathi Boningari and Panagiotis G Smirniotis. Impact of nitrogen oxides on the environment and human health: Mn-based materials for the nox abatement. *Current Opinion in Chemical Engineering*, 13:133–141, 2016.

[2] Janusz Lasek, Yi-Hui Yu, and Jeffrey C.S. Wu. Removal of nox by photocatalytic processes. *Journal of Photochemistry and Photobiology C: Photochemistry Reviews*, 14:29–52, 2013.

[3] Haihan Chen, Charith E. Nanayakkara, and Vicki H. Grassian. Titanium dioxide photocatalysis in atmospheric chemistry. *Chemical Reviews*, 112(11):5919–5948, 2012.

[4] Qingping Wu and Roel van de Krol. Selective photoreduction of nitric oxide to nitrogen by nanostructured tio2 photocatalysts: Role of oxygen vacancies and iron dopant. *Journal of the American Chemical Society*, 134(22):9369–9375, 2012. PMID: 22607604.

[5] Chenxi Guo, Xiaoyan Fu, Jun Long, Huan Li, Gangqiang Qin, Ang Cao, Huijuan Jing, and Jianping Xiao. Toward computational design of chemical reactions with reaction phase diagram. *WIREs Computational Molecular Science*, n/a(n/a):e1514, jan 2021.

[6] Xu Zong and Can Li. 7 - Photocatalytic water splitting on metal oxide-based semiconductor photocatalysts. In Jacques C B T Metal Oxides in Heterogeneous Catalysis Védrine, editor, *Metal Oxides*, pages 355–399. Elsevier, 2018.

[7] Pu Guo, Xiaoyan Fu, Peter Deák, Thomas Frauenheim, and Jianping Xiao. Activity and Mechanism Mapping of Photocatalytic NO 2 Conversion on the Anatase TiO 2 (101) Surface. *The Journal of Physical Chemistry Letters*, 12(32):7708–7716, aug 2021.

[8] Zhendong Guo, Francesco Ambrosio, Wei Chen, Patrick Gono, and Alfredo Pasquarello. Alignment of Redox Levels at Semiconductor–Water Interfaces. *Chemistry of Materials*, 30(1):94–111, jan 2018.

[9] Sounak Roy, M.S. Hegde, and Giridhar Madras. Catalysis for nox abatement. *Applied Energy*, 86(11):2283–2297, 2009.

[10] Fredrik Normann, Klas Andersson, Bo Leckner, and Filip Johnsson. Emission control of nitrogen oxides in the oxy-fuel process. *Progress in Energy and Combustion Science*, 35(5):385–397, 2009.

[11] Konrad Stemmler, Markus Ammann, Chantal Donders, Jörg Kleffmann, and Christian George. Photosensitized reduction of nitrogen dioxide on humic acid as a source of nitrous acid. *Nature*, 440(7081):195–198, 2006.

[12] Jan Haubrich, Ryan G. Quiller, Lauren Benz, Zhi Liu, and Cynthia M. Friend. In situ ambient pressure studies of the chemistry of no2 and water on rutile tio2(110). *Langmuir*, 26(4):2445–2451, February 2010.

[13] M.M. Ballari, M. Hunger, G. Hüsken, and H.J.H. Brouwers. Modelling and experimental study of the nox photocatalytic degradation employing concrete pavement with titanium dioxide. *Catalysis Today*, 151(1):71–76, 2010.

[14] Jonathan Z. Bloh, Ralf Dillert, and Detlef W. Bahnemann. Ruthenium-modified zinc oxide, a highly active vis-photocatalyst: the nature and reactivity of photoactive centres. *Phys. Chem. Chem. Phys.*, 16:5833–5845, 2014.

[15] Yu Mao, Ziyun Wang, Hai-Feng Wang, and P. Hu. Understanding catalytic reactions over zeolites: A density functional theory study of selective catalytic reduction of nox by nh3 over cu-sapo-34. *ACS Catal.*, 6(11):7882–7891, November 2016.

[16] Ilias Papailias, Nadia Todorova, Tatiana Giannakopoulou, Jiaguo Yu, Dimitra Dimotikali, and Christos Trapalis. Photocatalytic activity of modified g-c3n4/tio2 nanocomposites for nox removal. *Catalysis Today*, 280:37–44, 2017.

[17] Jingguang G. Chen, Richard M. Crooks, Lance C. Seefeldt, Kara L. Bren, R. Morris Bullock, Marcetta Y. Darensbourg, Patrick L. Holland, Brian Hoffman, Michael J. Janik, Anne K. Jones, Mercouri G. Kanatzidis, Paul King, Kyle M. Lancaster, Sergei V. Lymar, Peter Pfromm, William F. Schneider, and Richard R. Schrock. Beyond fossil fuel–driven nitrogen transformations. *Science*, 360(6391), 2018.

[18] F. L. Toma, G. Bertrand, D. Klein, and C. Coddet. Photocatalytic removal of nitrogen oxides via titanium dioxide. *Environmental Chemistry Letters*, 2(3):117–121, Dec 2004.

[19] Neil Bowering and Deborah Croston. Silver modified degussa p25 for the photocatalytic removal of nitric oxide. *International Journal of Photoenergy*, 2007.

[20] Ambarish Kulkarni, Samira Siahrostami, Anjli Patel, and Jens K Nørskov. Understanding Catalytic Activity Trends in the Oxygen Reduction Reaction. *Chemical Reviews*, 118(5):2302–2312, mar 2018.

[21] Andrew J Medford, Chuan Shi, Max J Hoffmann, Adam C Lausche, Sean R Fitzgibbon, Thomas Bligaard, and Jens K Nørskov. CatMAP: A Software Package for Descriptor-Based Microkinetic Mapping of Catalytic Trends. *Catalysis Letters*, 145(3):794–807, 2015.

[22] J. K. Nørskov, J. Rossmeisl, A. Logadottir, L. Lindqvist, J. R. Kitchin, T. Bligaard, and H. Jónsson. Origin of the overpotential for oxygen reduction at a fuel-cell cathode. *J. Phys. Chem. B*, 108(46):17886–17892, November 2004.

[23] E.M. Fernandez, P.G. Moses, A. Toftelund, H.A. Hansen andJ.I. Martínez, F. Abild-Pedersen, J. Kleis, B. Hinnemann, J. Rossmeisl, T. Bligaard, and J.K. Nørskov. Scaling relationships for adsorption energies on transition metal oxide, sulfide, and nitride surfaces. *Angewandte Chemie International Edition*, 47:4683–4686, 2008.

[24] F. Abild-Pedersen, J. Greeley, F. Studt, J. Rossmeisl, T. R. Munter, P. G. Moses, E. Skúlason, T. Bligaard, and J. K. Nørskov. Scaling properties of adsorption energies for hydrogen-containing molecules on transition-metal surfaces. *Phys. Rev. Lett.*, 99:016105, Jul 2007.

[25] Andrew A. Peterson and Jens K. Nørskov. Activity descriptors for co2 electroreduction to methane on transition-metal catalysts. *J. Phys. Chem. Lett.*, 3(2):251–258, January 2012.

[26] Zheng Zhang, Jianping Xiao, Xue-Jiao Chen, Song Yu, Liang Yu, Rui Si, Yong Wang, Suheng Wang, Xianguang Meng, Ye Wang, Zhong-Qun Tian, and Dehui Deng. Reaction Mechanisms of Well-Defined Metal–N4 Sites in Electrocatalytic CO2 Reduction. *Angewandte Chemie International Edition*, 57(50):16339–16342, 2018.

[27] Yanmei Shi, Yan Ji, Jun Long, Yu Liang, Yang Liu, Yifu Yu, Jianping Xiao, and Bin Zhang. Unveiling hydrocerussite as an electrochemically stable active phase for efficient carbon dioxide electroreduction to formate. *Nature Communications*, 11(1):3415, 2020.

[28] Bo Yang, Robbie Burch, Christopher Hardacre, Gareth Headdock, and P. Hu. Understanding the optimal adsorption energies for catalyst screening in heterogeneous catalysis. *ACS Catalysis*, 4(1):182–186, 2014.

[29] Ziyun Wang, Hai-Feng Wang, and P. Hu. Possibility of designing catalysts beyond the traditional volcano curve: a theoretical framework for multi-phase surfaces. *Chem. Sci.*, 6:5703–5711, 2015.

[30] T. Bligaard, J.K. Nørskov, S. Dahl, J. Matthiesen, C.H. Christensen, and J. Sehested. The brønsted? @ sevans? @ spolanyi relation and the volcano curve in heterogeneous catalysis. *Journal of Catalysis*, 224(1):206–217, 2004.

[31] Jian-Fu Chen, Yu Mao, Hai-Feng Wang, and P. Hu. Reversibility iteration method for understanding reaction networks and for solving microkinetics in heterogeneous catalysis. *ACS Catalysis*, 6(10):7078–7087, 2016.

[32] Xinyan Liu, Jianping Xiao, Hongjie Peng, Xin Hong, Karen Chan, and Jens K Nørskov. Understanding trends in electrochemical carbon dioxide reduction rates. *Nature Communications*, 8(1):15438, 2017.

[33] Jun Long, Shiming Chen, Yunlong Zhang, Chenxi Guo, Xiaoyan Fu, Dehui Deng, and Jianping Xiao. Direct Electrochemical Ammonia Synthesis from Nitric Oxide. *Angewandte Chemie (International ed. in English)*, 59(24):9711–9718, jun 2020.

[34] Yanmei Shi, Yan Ji, Jun Long, Yu Liang, Yang Liu, Yifu Yu, Jianping Xiao, and Bin Zhang. Unveiling hydrocerussite as an electrochemically stable active phase for efficient carbon dioxide electroreduction to formate. *Nature Communications*, 11(1):3415, 2020.

[35] Antonio Tilocca and Annabella Selloni. Structure and Reactivity of Water Layers on Defect-Free and Defective Anatase TiO2(101) Surfaces. *The Journal of Physical Chemistry B*, 108(15):4743–4751, apr 2004.

[36] Peter Deák, Bálint Aradi, and Thomas Frauenheim. Quantitative theory of the oxygen vacancy and carrier self-trapping in bulk tio_2. *Phys. Rev. B*, 86:195206, Nov 2012.

[37] Philipp Scheiber, Martin Fidler, Olga Dulub, Michael Schmid, Ulrike Diebold, Weiyi Hou, Ulrich Aschauer, and Annabella Selloni. (sub)surface mobility of oxygen vacancies at the tio_2 anatase (101) surface. *Phys. Rev. Lett.*, 109:136103, Sep 2012.

[38] Martin Setvin, Cesare Franchini, Xianfeng Hao, Michael Schmid, Anderson Janotti, Merzuk Kaltak, Chris G. Van de Walle, Georg Kresse, and Ulrike Diebold. Direct view at excess electrons in tio_2 rutile and anatase. *Phys. Rev. Lett.*, 113:086402, Aug 2014.

[39] Ulrich Aschauer, Yunbin He, Hongzhi Cheng, Shao-Chun Li, Ulrike Diebold, and Annabella Selloni. Influence of Subsurface Defects on the Surface Reactivity of TiO2: Water on Anatase (101). *The Journal of Physical Chemistry C*, 114(2):1278–1284, jan 2010.

[40] Martin Setvin, Xianfeng Hao, Benjamin Daniel, Jiri Pavelec, Zbynek Novotny, Gareth S. Parkinson, Michael Schmid, Georg Kresse, Cesare Franchini, and Ulrike Diebold. Charge Trapping at the Step Edges of TiO 2 Anatase (101). *Angewandte Chemie International Edition*, 53(18):4714–4716, apr 2014.

[41] Sencer Selcuk and Annabella Selloni. Facet-dependent trapping and dynamics of excess electrons at anatase TiO2 surfaces and aqueous interfaces. *Nature Materials*, 15(10):1107–1112, oct 2016.

[42] S. Moser, L. Moreschini, J. Jaćimović, O. S. Barišić, H. Berger, A. Magrez, Y. J. Chang, K. S. Kim, A. Bostwick, E. Rotenberg, L. Forró, and M. Grioni. Tunable polaronic conduction in anatase tio_2. *Phys. Rev. Lett.*, 110:196403, May 2013.

[43] Dong Wang, Tian Sheng, Jianfu Chen, Hai Feng Wang, and P. Hu. Identifying the key obstacle in photocatalytic oxygen evolution on rutile TiO2. *Nature Catalysis*, 1(4):291–299, 2018.

[44] Christoph Freysoldt, Blazej Grabowski, Tilmann Hickel, Jörg Neugebauer, Georg Kresse, Anderson Janotti, and Chris G Van de Walle. First-principles calculations for point defects in solids. *Reviews of Modern Physics*, 86(1):253–305, mar 2014.

[45] Hannu-Pekka Komsa and Alfredo Pasquarello. Finite-Size Supercell Correction for Charged Defects at Surfaces and Interfaces. *Physical Review Letters*, 110(9):95505, feb 2013.

[46] Meisam Farzalipour Tabriz, Bálint Aradi, Thomas Frauenheim, and Peter Deák. Application of the Lany–Zunger polaron correction for calculating surface charge trapping. *Journal of Physics: Condensed Matter*, 29(39):394001, 2017.

[47] Meisam Farzalipour Tabriz, Bálint Aradi, Thomas Frauenheim, and Peter Deák. SLABCC: Total energy correction code for charged periodic slab models. *Computer Physics Communications*, 240:101–105, 2019.

[48] Mauricio Chagas da Silva, Michael Lorke, Bálint Aradi, Meisam Farzalipour Tabriz, Thomas Frauenheim, Angel Rubio, Dario Rocca, and Peter Deák. Self-consistent potential correction for charged periodic systems. *Phys. Rev. Lett.*, 126:076401, Feb 2021.

[49] AKIRA FUJISHIMA and KENICHI HONDA. Electrochemical Photolysis of Water at a Semiconductor Electrode. *Nature*, 238(5358):37–38, 1972.

[50] Vinodkumar Etacheri, Cristiana Di Valentin, Jenny Schneider, Detlef Bahnemann, and Suresh C. Pillai. Visible-light activation of tio2 photocatalysts: Advances in theory and experiments. *Journal of Photochemistry and Photobiology C: Photochemistry Reviews*, 25:1–29, 2015.

[51] Jan Augustynski. The role of the surface intermediates in the photoelectrochemical behaviour of anatase and rutile tio2. *Electrochimica Acta*, 38(1):43–46, 1993.

[52] Teruhisa Ohno, Koji Sarukawa, and Michio Matsumura. Crystal faces of rutile and anatase tio2 particles and their roles in photocatalytic reactions. *New J. Chem.*, 26:1167–1170, 2002.

[53] Suzuko Yamazaki, Saori Matsunaga, and Kenzi Hori. Photocatalytic degradation of trichloroethylene in water using tio2 pellets. *Water Research*, 35(4):1022–1028, 2001.

[54] Michele Lazzeri, Andrea Vittadini, and Annabella Selloni. Structure and energetics of stoichiometric $\mathrm{tio_2}$ anatase surfaces. *Phys. Rev. B*, 63:155409, Mar 2001.

[55] Antonio Tilocca and Annabella Selloni. Reaction pathway and free energy barrier for defect-induced water dissociation on the (101) surface of TiO2-anatase. *The Journal of Chemical Physics*, 119(14):7445–7450, sep 2003.

[56] Ye-Fei Li and Annabella Selloni. Theoretical Study of Interfacial Electron Transfer from Reduced Anatase TiO2(101) to Adsorbed O2. *Journal of the American Chemical Society*, 135(24):9195–9199, jun 2013.

[57] Xiaoyang Pan, Min-Quan Yang, Xianzhi Fu, Nan Zhang, and Yi-Jun Xu. Defective tio2 with oxygen vacancies: synthesis, properties and photocatalytic applications. *Nanoscale*, 5:3601–3614, 2013.

[58] Martin Setvin, Ulrich Aschauer, Jan Hulva, Thomas Simschitz, Benjamin Daniel, Michael Schmid, Annabella Selloni, and Ulrike Diebold. Following the Reduction of Oxygen on TiO2 Anatase (101) Step by Step. *Journal of the American Chemical Society*, 138(30):9565–9571, aug 2016.

[59] M K Nowotny, L R Sheppard, T Bak, and J Nowotny. Defect Chemistry of Titanium Dioxide. Application of Defect Engineering in Processing of TiO2-Based Photocatalysts. *The Journal of Physical Chemistry C*, 112(14):5275–5300, apr 2008.

[60] Peter Deák, Bálint Aradi, and Thomas Frauenheim. Quantitative theory of the oxygen vacancy and carrier self-trapping in bulk TiO_2. *Physical Review B*, 86(19):195206, nov 2012.

[61] Max C. Holthausen Wolfram Koch. *A Chemist's Guide to Density Functional Theory. Decond Edition*. Wiley-VCH Verlag GmbH, 2001.

[62] L. Pauling and Jr. E. B. Wilson. *Introduction to Quantum Mechanics with Applications to Chemistry*. Dover Publications, 1963.

[63] Max Born; J. Robert Oppenheimer. Zur quantentheorie der molekeln. *Annalen der Physik (in German)*, 20, 1927.

[64] P A M Dirac. Quantum Mechanics of Many-Electron Systems. *Proceedings of the Royal Society of London. Series A, Containing Papers of a Mathematical and Physical Character*, 123(792):714–733, jun 1929.

[65] D R Hartree. The Wave Mechanics of an Atom with a Non-Coulomb Central Field. Part II. Some Results and Discussion. *Mathematical Proceedings of the Cambridge Philosophical Society*, 24(1):111–132, 1928.

[66] J. C. Slater. Note on hartree's method. *Phys. Rev.*, 35:210–211, Jan 1930.

[67] V Fock. Näherungsmethode zur Lösung des quantenmechanischen Mehrkörperproblems. *Zeitschrift für Physik*, 61(1):126–148, 1930.

[68] P. Hohenberg and W. Kohn. Inhomogeneous electron gas. *Phys. Rev.*, 136:B864–B871, Nov 1964.

[69] W. Kohn and L. J. Sham. Self-consistent equations including exchange and correlation effects. *Phys. Rev.*, 140:A1133–A1138, Nov 1965.

[70] W. Kohn. Nobel lecture: Electronic structure of matter—wave functions and density functionals. *Rev. Mod. Phys.*, 71:1253–1266, Oct 1999.

[71] M. Fuchs, M. Bockstedte, E. Pehlke, and M. Scheffler. Pseudopotential study of binding properties of solids within generalized gradient approximations: The role of core-valence exchange correlation. *Phys. Rev. B*, 57:2134–2145, Jan 1998.

[72] B. Hammer, L. B. Hansen, and J. K. Nørskov. Improved adsorption energetics within density-functional theory using revised perdew-burke-ernzerhof functionals. *Phys. Rev. B*, 59:7413–7421, Mar 1999.

[73] Jochen Heyd, Gustavo E Scuseria, and Matthias Ernzerhof. Hybrid functionals based on a screened Coulomb potential. *The Journal of Chemical Physics*, 118(18):8207–8215, apr 2003.

[74] Aron J Cohen, Paula Mori-Sánchez, and Weitao Yang. Challenges for Density Functional Theory. *Chemical Reviews*, 112(1):289–320, jan 2012.

[75] Christoph Freysoldt, Blazej Grabowski, Tilmann Hickel, Jörg Neugebauer, Georg Kresse, Anderson Janotti, and Chris G. Van de Walle. First-principles calculations for point defects in solids. *Rev. Mod. Phys.*, 86:253–305, Mar 2014.

[76] Peter Deák, Bálint Aradi, and Thomas Frauenheim. Polaronic effects in tio_2 calculated by the hse06 hybrid functional: Dopant passivation by carrier self-trapping. *Phys. Rev. B*, 83:155207, Apr 2011.

[77] Jochen Heyd, Gustavo E. Scuseria, and Matthias Ernzerhof. Hybrid functionals based on a screened coulomb potential. *The Journal of Chemical Physics*, 118(18):8207–8215, 2003.

[78] Stephan Lany and Alex Zunger. Polaronic hole localization and multiple hole binding of acceptors in oxide wide-gap semiconductors. *Phys. Rev. B*, 80:085202, Aug 2009.

[79] Stephan Lany and Alex Zunger. Assessment of correction methods for the band-gap problem and for finite-size effects in supercell defect calculations: Case studies for zno and gaas. *Phys. Rev. B*, 78:235104, Dec 2008.

[80] Feng Xiong, Li-Li Yin, Zhengming Wang, Yuekang Jin, Guanghui Sun, Xue-Qing Gong, and Weixin Huang. Surface reconstruction-induced site-specific charge separation and photocatalytic reaction on anatase tio2(001) surface. *The Journal of Physical Chemistry C*, 121(18):9991–9999, 2017.

[81] Feng Xiong, Li-Li Yin, Fei Li, Zongfang Wu, Zhengming Wang, Guanghui Sun, Hong Xu, Peng Chai, Xue-Qing Gong, and Weixin Huang. Anatase TiO2(001)-(1 × 4) Surface Is Intrinsically More Photocatalytically Active than the Rutile TiO2(110)-(1 × 1) Surface. *The Journal of Physical Chemistry C*, 123(40):24558–24565, oct 2019.

[82] Jun Cheng, Joost VandeVondele, and Michiel Sprik. Identifying trapped electronic holes at the aqueous tio2 interface. *The Journal of Physical Chemistry C*, 118(10):5437–5444, 2014.

[83] Raina Wanbayor, Peter Deák, Thomas Frauenheim, and Vithaya Ruangpornvisuti. First principles theoretical study of the hole-assisted conversion of CO to CO2 on the anatase TiO2(101) surface. *The Journal of Chemical Physics*, 134(10):104701, mar 2011.

[84] Jessica Scaranto and Santi Giorgianni. A quantum-mechanical study of CO adsorbed on TiO2: A comparison of the Lewis acidity of the rutile (110) and the anatase (101) surfaces. *Journal of Molecular Structure: THEOCHEM*, 858(1):72–76, 2008.

[85] Dorothee Stodt, Heshmat Noei, Christof Hättig, and Yuemin Wang. A combined experimental and computational study on the adsorption and reactions of no on rutile tio2. *Phys. Chem. Chem. Phys.*, 15:466–472, 2013.

[86] Daniel Berger, Harald Oberhofer, and Karsten Reuter. First-principles embedded-cluster calculations of the neutral and charged oxygen vacancy at the rutile $\mathrm{tio_2}$(110) surface. *Phys. Rev. B*, 92:075308, Aug 2015.

[87] Hannu-Pekka Komsa and Alfredo Pasquarello. Finite-size supercell correction for charged defects at surfaces and interfaces. *Phys. Rev. Lett.*, 110:095505, Feb 2013.

[88] Christoph Freysoldt, Jörg Neugebauer, and Chris G. Van de Walle. Fully ab initio finite-size corrections for charged-defect supercell calculations. *Phys. Rev. Lett.*, 102:016402, Jan 2009.

[89] Fabien Devynck, Audrius Alkauskas, Peter Broqvist, and Alfredo Pasquarello. Charge transition levels of carbon-, oxygen-, and hydrogen-related defects at the sic/$\mathrm{sio_2}$ interface through hybrid functionals. *Phys. Rev. B*, 84:235320, Dec 2011.

[90] Jan Felix Binder, Peter Broqvist, Hannu-Pekka Komsa, and Alfredo Pasquarello. Germanium core-level shifts at ge/$\mathrm{geo_2}$ interfaces through hybrid functionals. *Phys. Rev. B*, 85:245305, Jun 2012.

[91] Talin Avanesian and Phillip Christopher. Scaled Degree of Rate Control: Identifying Elementary Steps That Control Differences in Performance of Transition-Metal Catalysts. *ACS Catalysis*, 6(8):5268–5272, aug 2016.

[92] Haiyang Yuan, Ningning Sun, Jianfu Chen, Jiamin Jin, Haifeng Wang, and Peijun Hu. Insight into the NH3-Assisted Selective Catalytic Reduction of NO on

β-MnO2(110): Reaction Mechanism, Activity Descriptor, and Evolution from a Pristine State to a Steady State. *ACS Catalysis*, 8(10):9269–9279, 2018.

[93] Carsten Stegelmann, Anders Andreasen, and Charles T Campbell. Degree of Rate Control: How Much the Energies of Intermediates and Transition States Control Rates. *Journal of the American Chemical Society*, 131(23):8077–8082, jun 2009.

[94] Zhongtian Mao and Charles T Campbell. The degree of rate control of catalyst-bound intermediates in catalytic reaction mechanisms: Relationship to site coverage. *Journal of Catalysis*, 381:53–62, 2020.

[95] Chen Jianfu, Jia Menglei, Hu Peijun, and Haifeng Wang. Catkinas: A large-scale catalytic microkinetic analysis software for mechanism auto-analysis and catalyst screening. *J. Comput. Chem.*, 2021.

[96] Vei Wang, Nan Xu, Jin-Cheng Liu, Gang Tang, and Wen-Tong Geng. Vaspkit: A user-friendly interface facilitating high-throughput computing and analysis using vasp code. *Computer Physics Communications*, 267:108033, 2021.

[97] Simon K. Beaumont, R. Joel Gustafsson, and Richard M. Lambert. Heterogeneous photochemistry relevant to the troposphere: H2o2 production during the photochemical reduction of no2 to hono on uv-illuminated tio2 surfaces. *Chem.Phys.Chem*, 10(2):331–333, Feb 2009.

[98] Graeme Henkelman, Blas P. Uberuaga, and Hannes Jónsson. A climbing image nudged elastic band method for finding saddle points and minimum energy paths. *The Journal of Chemical Physics*, 113(22):9901–9904, 2000.

[99] Andreas Heyden, Alexis T. Bell, and Frerich J. Keil. Efficient methods for finding transition states in chemical reactions: Comparison of improved dimer method and partitioned rational function optimization method. *The Journal of Chemical Physics*, 123(22):224101, 2005.

[100] Graeme Henkelman and Hannes Jónsson. Improved tangent estimate in the nudged elastic band method for finding minimum energy paths and saddle points. *The Journal of Chemical Physics*, 113(22):9978–9985, 2000.

[101] Graeme Henkelman and Hannes Jónsson. A dimer method for finding saddle points on high dimensional potential surfaces using only first derivatives. *The Journal of Chemical Physics*, 111(15):7010–7022, 1999.

[102] John P. Perdew, Kieron Burke, and Matthias Ernzerhof. Generalized gradient approximation made simple. *Phys. Rev. Lett.*, 77:3865–3868, Oct 1996.

[103] G. Kresse and J. Hafner. Ab initio molecular dynamics for liquid metals. *Phys. Rev. B*, 47:558–561, Jan 1993.

[104] G. Kresse and J. Hafner. Ab initio molecular-dynamics simulation of the liquid-metal–amorphous-semiconductor transition in germanium. *Phys. Rev. B*, 49:14251–14269, May 1994.

[105] G. Kresse and J. Furthmüller. Efficiency of ab-initio total energy calculations for metals and semiconductors using a plane-wave basis set. *Computational Materials Science*, 6(1):15–50, 1996.

[106] Benjamin J Morgan and Graeme W Watson. A DFT+U description of oxygen vacancies at the TiO2 rutile (110) surface. *Surface Science*, 601(21):5034–5041, 2007.

[107] Konstantin Hadjiivanov, V. Bushev, Margarita Kantcheva, and Dimitar Klissurski. Infrared spectroscopy study of the species arising during nitrogen dioxide adsorption on titania (anatase). *Langmuir*, 10(2):464–471, February 1994.

[108] G. M. Underwood, T. M. Miller, and V. H. Grassian. Transmission ft-ir and knudsen cell study of the heterogeneous reactivity of gaseous nitrogen dioxide on mineral oxide particles. *J. Phys. Chem. A*, 103(31):6184–6190, August 1999.

[109] Yuri Bedjanian and Atallah El Zein. Interaction of no2 with tio2 surface under uv irradiation: Products study. *J. Phys. Chem. A*, 116(7):1758–1764, Feb 2012.

[110] Courtney R. Usher, Amy E. Michel, and Vicki H. Grassian. Reactions on mineral dust. *Chem. Rev.*, 103(12):4883–4940, December 2003.

[111] Y. Dubowski, A. L. Sumner, E. J. Menke, D. J. Gaspar, J. T. Newberg, R. C. Hoffman, R. M. Penner, J. C. Hemminger, and B. J. Finlayson-Pitts. Interactions of gaseous nitric acid with surfaces of environmental interest. *Phys. Chem. Chem. Phys.*, 6:3879–3888, 2004.

[112] Kevin A. Ramazan, Dennis Syomin, and Barbara J. Finlayson-Pitts. The photochemical production of hono during the heterogeneous hydrolysis of no2. *Phys. Chem. Chem. Phys.*, 6:3836–3843, 2004.

[113] Dennis A. Syomin and Barbara J. Finlayson-Pitts. Hono decomposition on borosilicate glass surfaces: implications for environmental chamber studies and field experiments. *Phys. Chem. Chem. Phys.*, 5:5236–5242, 2003.

[114] R. Joel Gustafsson, Georgios Kyriakou, and Richard M. Lambert. The molecular mechanism of tropospheric nitrous acid production on mineral dust surfaces. *ChemPhysChem*, 9(10):1390–1393, July 2008.

[115] Jan Haubrich, Ryan G. Quiller, Lauren Benz, Zhi Liu, and Cynthia M. Friend. In situ ambient pressure studies of the chemistry of no2 and water on rutile tio2(110). *Langmuir*, 26(4):2445–2451, 2010. PMID: 20070108.

[116] A L Goodman, G M Underwood, and V H Grassian. Heterogeneous Reaction of NO2: Characterization of Gas-Phase and Adsorbed Products from the Reaction, 2NO2(g) + H2O(a) → HONO(g) + HNO3(a) on Hydrated Silica Particles. *The Journal of Physical Chemistry A*, 103(36):7217–7223, sep 1999.

[117] Wei-Na Zhao and Zhi-Pan Liu. Mechanism and active site of photocatalytic water splitting on titania in aqueous surroundings. *Chem. Sci.*, 5(6):2256–2264, 2014.

[118] Li-Min Liu, Paul Crawford, and P Hu. The interaction between adsorbed OH and O2 on TiO2 surfaces. *Progress in Surface Science*, 84(5):155–176, 2009.

[119] Masakazu Anpo, Norikazu Aikawa, Yutaka Kubokawa, Michel Che, Catherine Louis, and Elio Giamello. Photoluminescence and photocatalytic activity of highly dispersed titanium oxide anchored onto porous vycor glass. *The Journal of Physical Chemistry*, 89(23):5017–5021, 1985.

[120] Masakazu. Anpo, Takahito. Shima, Sukeya. Kodama, and Yutaka. Kubokawa. Photocatalytic hydrogenation of propyne with water on small-particle titania: size quantization effects and reaction intermediates. *The Journal of Physical Chemistry*, 91(16):4305–4310, 1987.

[121] Masakazu Anpo and Masato Takeuchi. The design and development of highly reactive titanium oxide photocatalysts operating under visible light irradiation. *Journal of Catalysis*, 216(1):505–516, 2003. 40th Anniversary Commemorative Issue.

[122] Masakazu Anpo, Tae-Ho Kim, and Masaya Matsuoka. The design of ti-, v-, cr-oxide single-site catalysts within zeolite frameworks and their photocatalytic reactivity for the decomposition of undesirable molecules? @ tthe role of their excited states and reaction mechanisms. *Catalysis Today*, 142(3):114–124, 2009. Selected Papers from the 6th International Symposium on Group Five Elements, Pozna? D, Poland, 7-10 May, 2008.

[123] Yunjun Cao, Min Yu, Shandong Qi, Zhengfeng Ren, Shishen Yan, Shujun Hu, and Mingchun Xu. Nitric oxide reaction pathways on rutile tio2(110): The influence of surface defects and reconstructions. *The Journal of Physical Chemistry C*, 122(41):23441–23450, 2018.

[124] Xiaoyan Fu, Jiayi Li, Jun Long, Chenxi Guo, and Jianping Xiao. Understanding the Product Selectivity of Syngas Conversion on ZnO Surfaces with Complex Reaction Network and Structural Evolution. *ACS Catalysis*, 11(19):12264–12273, oct 2021.

[125] Taizo Shibuya, Kenji Yasuoka, Susanne Mirbt, and Biplab Sanyal. Bipolaron formation induced by oxygen vacancy at rutile tio2(110) surfaces. *The Journal of Physical Chemistry C*, 118(18):9429–9435, 2014.

[126] R. Schaub, P. Thostrup, N. Lopez, E. Lægsgaard, I. Stensgaard, J. K. Nørskov, and F. Besenbacher. Oxygen vacancies as active sites for water dissociation on rutile TiO2(110). *Physical Review Letters*, 87(26):266104–1–266104–4, dec 2001.

[127] Tracy L Thompson and John T Yates. TiO2-based Photocatalysis: Surface Defects, Oxygen and Charge Transfer. *Topics in Catalysis*, 35(3-4):197–210, jul 2005.

Appendices

A | Total energies corrections for charged systems

System with a postive charge	Adsorption energies (corrections)	
	SLABCC	SCPC
$Ti_{5c}{}^{perfect}$ + NO	2.48 eV (-0.01 eV)	2.54 eV (0.05 eV)
$O_{br}{}^{perfect}$ +NO	1.56 eV (-0.03 eV)	1.62 eV (0.03 eV)
$Ti_{5c}{}^{defective}$+ NO	2.52 eV (0.00 eV)	2.70 eV (0.18 eV)
$O_{br}{}^{defective}$+ NO	2.89 eV (0.00 eV	2.96 eV (0.07 eV)
$Ti_{5c}{}^{perfect}$ + OH	0.37 eV (-0.03 eV)	0.37 eV (-0.03 eV)
$Ti_{5c}{}^{defective}$ + OH	-1.32 eV (-0.11 eV)	-1.31 eV (-0.10 eV)

Table A.1 Charge correction to adsorption energies with SLABCC and SCPC methods in deNO$_2$ process.

Active sites	Free adsorption energy (eV)	
	without corrections	with SCPC correction
A-$Ti_{5c}^{perfect}$	1.28	1.48 (0.20)
R-$Ti_{5c}^{perfect}$	1.21	1.04 (-0.17)
A-Vo	1.06	0.86 (-0.20)
A-$Ti_{4c}^{defective}$	1.44	0.98 (-0.46)
A-$Ti_{5c}^{defective}$	1.48	1.74 (0.26)
R-Vo	1.35	0.91 (-0.44)
R-$Ti_{5c}^{defective}$	1.53	1.65 (0.12)

Table A.2 The corrected adsorption energies of O_2 (without ZPE and entropy corrections) over different sites of TiO_2 surfaces in deNO process.

B | Optimized geometries in the deNO$_2$ process

Here we display the optimized geometries of the N*, NO*, NO$_2$*, NO$_3$*, O*, O$_2$*, OH*, OOH*, H$_2$O*, H$_2$O$_2$* species adsorbed on the Vo, Ti$_{4c}$, Ti$_{5c}$ sites of the defective anatase TiO$_2$(101) surface and on the Ti$_{5c}$ site of the perfect anatase TiO$_2$(101) surface. We have also considered the Ti$_{5c}$(Vo) site in our calculations but the adsorbates tend to move to the Vo site from Ti$_{5c}$(Vo) site during the relaxation.

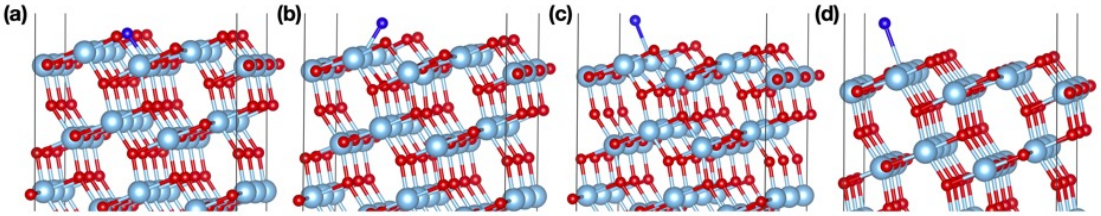

Fig. B.1 The optimized geometries of N adsorbed on the (a) Vo, (b) Ti$_{4c}$, (c) Ti$_{5c}$ sites of the defective surface and (d) on Ti$_{5c}$ of the perfect surface. Cyran, red, blue denotes Ti, O and N, respectively.

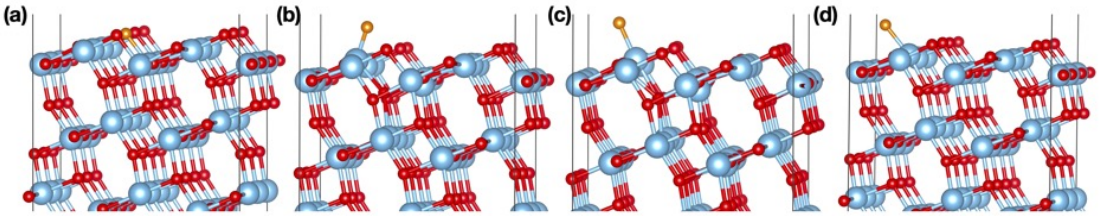

Fig. B.2 The optimized geometries of O adsorbed on the (a) Vo, (b) Ti$_{4c}$, (c) Ti$_{5c}$ sites of the defective surface and (d) on Ti$_{5c}$ of the perfect surface. Cyran, red, blue denotes Ti, O and N, respectively.

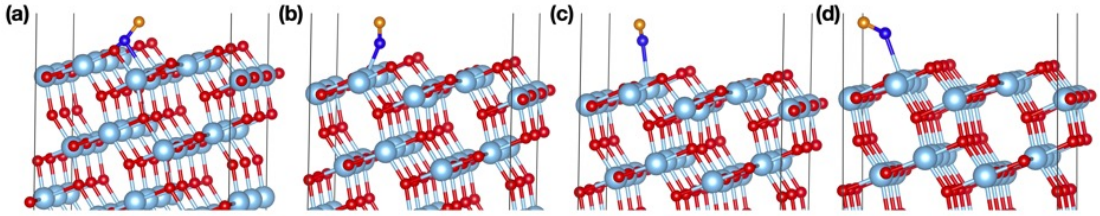

Fig. B.3 The optimized geometries of NO adsorbed on the (a) Vo, (b) Ti_{4c}, (c) Ti_{5c} sites of the defective surface and (d) on Ti_{5c} of the perfect surface. Cyran, red, blue denotes Ti, O and N, respectively.

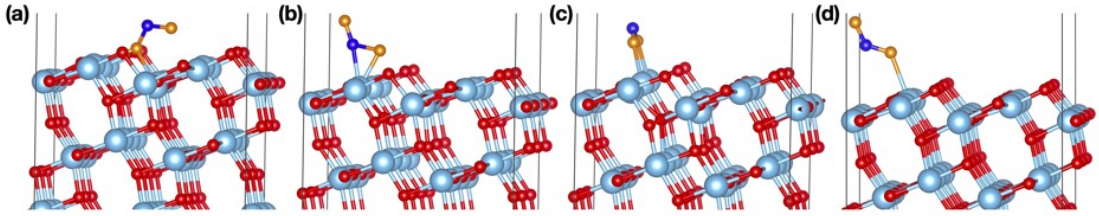

Fig. B.4 The optimized geometries of NO_2 adsorbed on the (a) Vo, (b) Ti_{4c}, (c) Ti_{5c} sites of the defective surface and (d) on Ti_{5c} of the perfect surface. Cyran, red, blue denotes Ti, O and N, respectively.

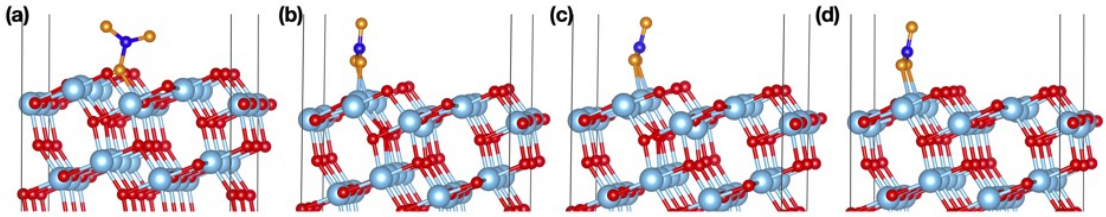

Fig. B.5 The optimized geometries of NO_3 adsorbed on the (a) Vo, (b) Ti_{4c}, (c) Ti_{5c} sites of the defective surface and (d) on Ti_{5c} of the perfect surface. Cyran, red, blue denotes Ti, O and N, respectively.

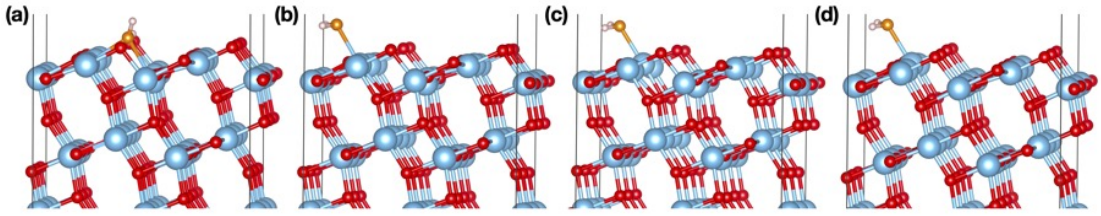

Fig. B.6 The optimized geometries of H_2O adsorbed on the (a) Vo, (b) Ti_{4c}, (c) Ti_{5c} sites of the defective surface and (d) on Ti_{5c} of the perfect surface. Cyran, red, blue denotes Ti, O and N, respectively.

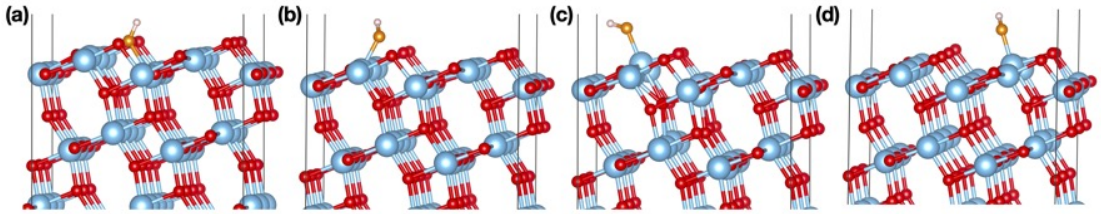

Fig. B.7 The optimized geometries of OH adsorbed on the (a) Vo, (b) Ti_{4c}, (c) Ti_{5c} sites of the defective surface and (d) on Ti_{5c} of the perfect surface. Cyran, red, blue denotes Ti, O and N, respectively.

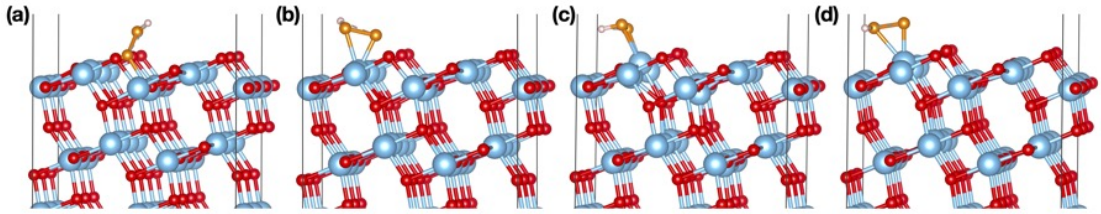

Fig. B.8 The optimized geometries of OOH adsorbed on the (a) Vo, (b) Ti_{4c}, (c) Ti_{5c} sites of the defective surface and (d) on Ti_{5c} of the perfect surface. Cyran, red, blue denotes Ti, O and N, respectively.

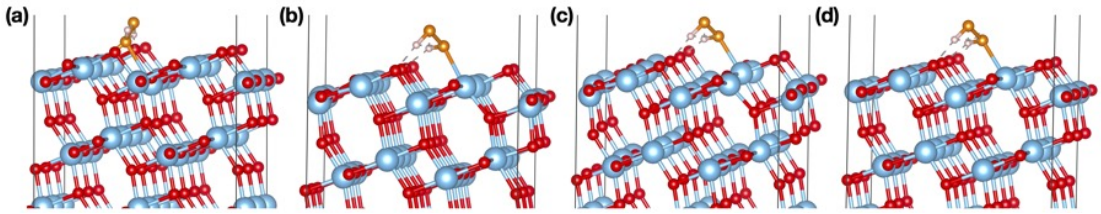

Fig. B.9 The optimized geometries of H_2O_2 adsorbed on the (a) Vo, (b) Ti_{4c}, (c) Ti_{5c} sites of the defective surface and (d) on Ti_{5c} of the perfect surface. Cyran, red, blue denotes Ti, O and N, respectively.

C | Optimized geometries in deNO process

Here we displayed the optimized geometries of the N*, O*, O_2*, N_2O*, N_2O_2* species adsorbed on the different sites of perfect and defective TiO_2 surfaces and Ti site of Y-zeolite(Ti-oxide).

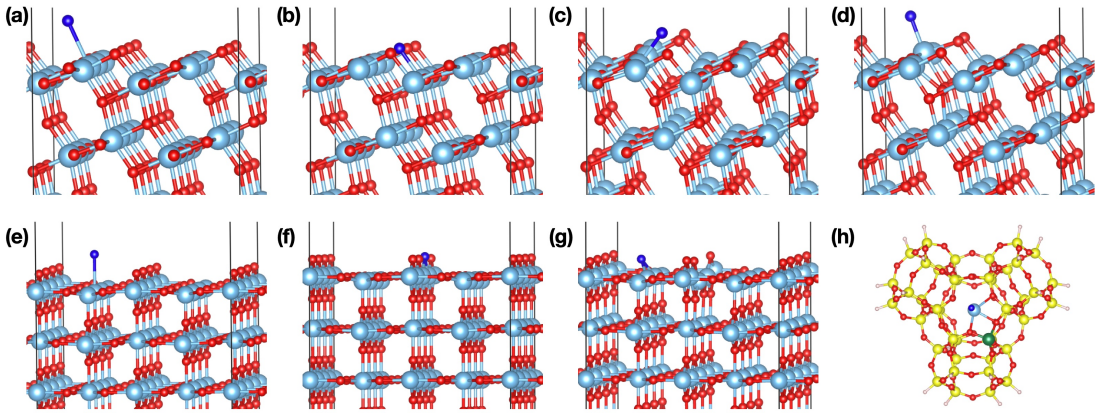

Fig. C.1 The optimized structures of N adsorbed on (a) Ti_{5c} of perfect anatase $TiO_2(101)$ surface, (b) oxygen vacancy(Vo) site of defective anatase $TiO_2(101)$ surface, (c) Ti_{4c} site of defective anatase $TiO_2(101)$ surface, (d)Ti_{5c} site of defective anatase $TiO_2(101)$ surface, (e)Ti_{5c} of perfect rutile $TiO_2(110)$ surface, (b) oxygen vacancy(Vo) site of defective rutile $TiO_2(110)$ surface, (c) Ti_{4c} site of defective rutile $TiO_2(110)$ surface, (d)Ti_{5c} site of defective rutile $TiO_2(110)$ surface

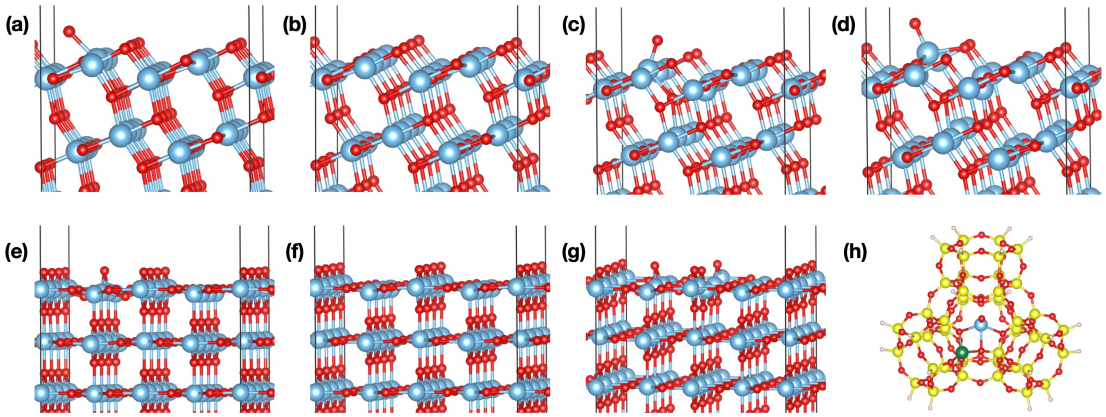

Fig. C.2 The optimized structures of O adsorbed on (a) Ti_{5c} of perfect anatase $TiO_2(101)$ surface, (b) oxygen vacancy(Vo) site of defective anatase $TiO_2(101)$ surface, (c) Ti_{4c} site of defective anatase $TiO_2(101)$ surface, (d)Ti_{5c} site of defective anatase $TiO_2(101)$ surface, (e)Ti_{5c} of perfect rutile $TiO_2(110)$ surface, (f) oxygen vacancy(Vo) site of defective rutile $TiO_2(110)$ surface, (g) Ti_{5c} site of defective rutile $TiO_2(110)$ surface, (h)Ti site of Ti-oxide Y-zeolite

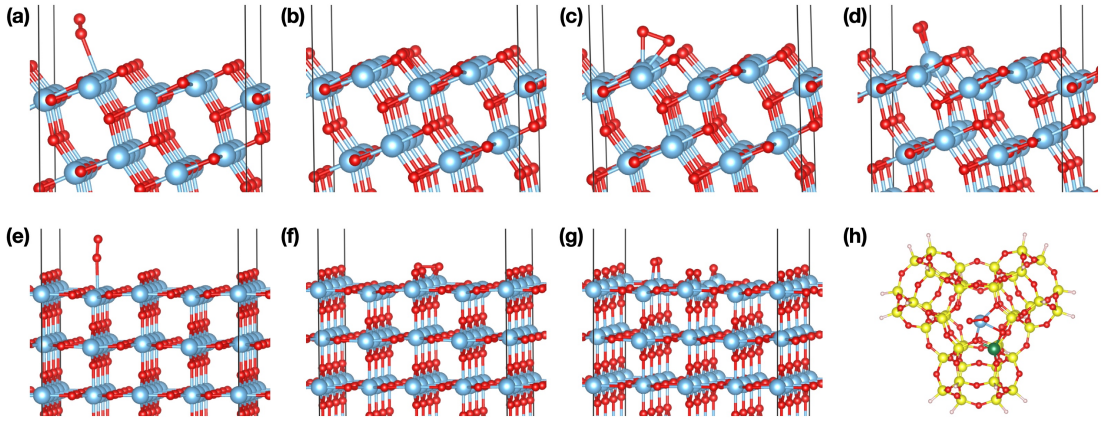

Fig. C.3 The optimized structures of O_2 adsorbed on (a) Ti_{5c} of perfect anatase $TiO_2(101)$ surface, (b) oxygen vacancy(Vo) site of defective anatase $TiO_2(101)$ surface, (c) Ti_{4c} site of defective anatase $TiO_2(101)$ surface, (d)Ti_{5c} site of defective anatase $TiO_2(101)$ surface, (e)Ti_{5c} of perfect rutile $TiO_2(110)$ surface, (f) oxygen vacancy(Vo) site of defective rutile $TiO_2(110)$ surface, (g) Ti_{5c} site of defective rutile $TiO_2(110)$ surface, (h)Ti site of Ti-oxide Y-zeolite

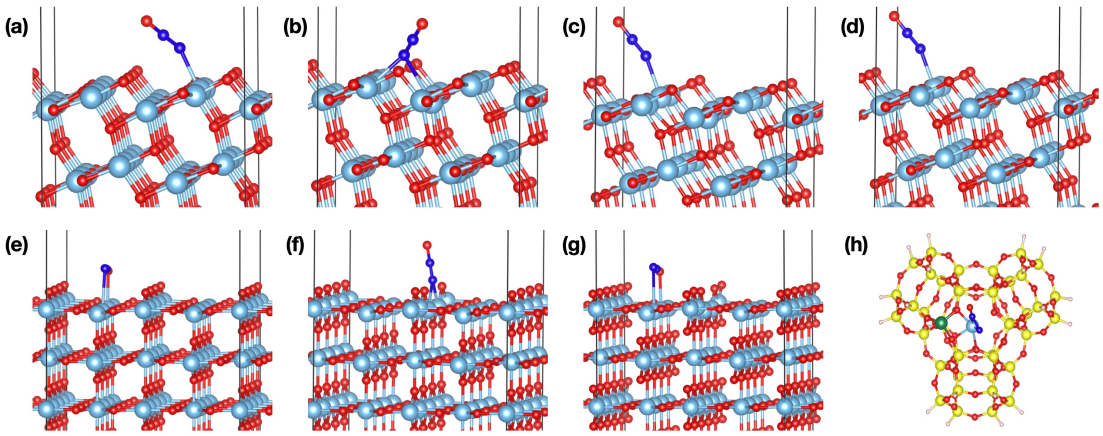

Fig. C.4 The optimized structures of N_2O adsorbed on (a) Ti_{5c} of perfect anatase $TiO_2(101)$ surface, (b) oxygen vacancy(Vo) site of defective anatase $TiO_2(101)$ surface, (c) Ti_{4c} site of defective anatase $TiO_2(101)$ surface, (d)Ti_{5c} site of defective anatase $TiO_2(101)$ surface, (e)Ti_{5c} of perfect rutile $TiO_2(110)$ surface, (f) oxygen vacancy(Vo) site of defective rutile $TiO_2(110)$ surface, (g) Ti_{5c} site of defective rutile $TiO_2(110)$ surface, (h)Ti site of Ti-oxide Y-zeolite

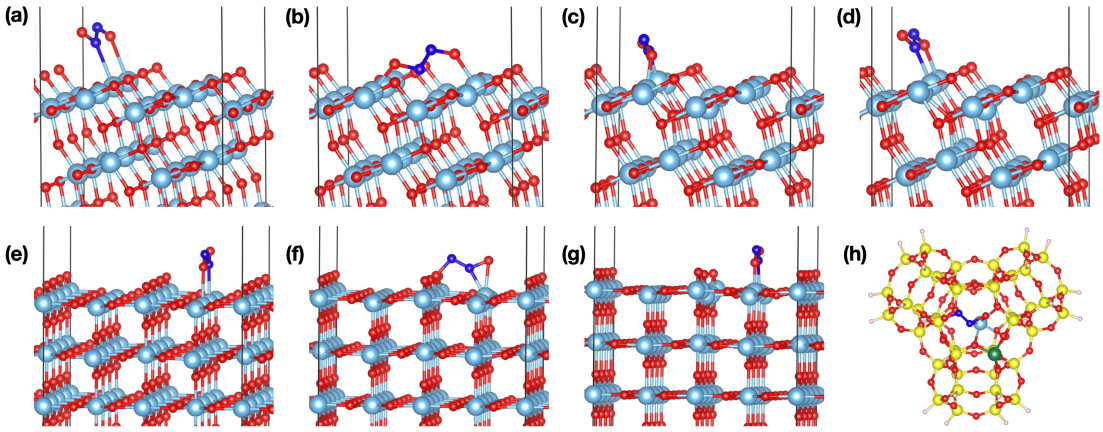

Fig. C.5 The optimized structures of N_2O_2 adsorbed on (a) Ti_{5c} of perfect anatase $TiO_2(101)$ surface, (b) oxygen vacancy(Vo) site of defective anatase $TiO_2(101)$ surface, (c) Ti_{4c} site of defective anatase $TiO_2(101)$ surface, (d)Ti_{5c} site of defective anatase $TiO_2(101)$ surface, (e)Ti_{5c} of perfect rutile $TiO_2(110)$ surface, (f) oxygen vacancy(Vo) site of defective rutile $TiO_2(110)$ surface, (g) Ti_{5c} site of defective rutile $TiO_2(110)$ surface, (h)Ti site of Ti-oxide Y-zeolite